

# Hierarchical Fluctuation Shapes a Dynamic Flow Linked to States of Consciousness

**Ang Li**

Institute of Biophysics, Chinese Academy of Sciences

**Haiyang Liu**

Capital Medical University

**Xu Lei**

Southwest University <https://orcid.org/0000-0003-2271-1287>

**Yini He**

Beijing Normal University

**Qian Wu**

Beijing Normal University <https://orcid.org/0000-0002-7469-1583>

**Yan Yan**

Shenzhen Institutes of Advanced Technology, Chinese Academy of Sciences

**Xin Zhou**

Beijing Normal University

**Xiaohan Tian**

Beijing Normal University

**Yingjie Peng**

Institute of Biophysics, Chinese Academy of Sciences

**Hao Yan**

Institute of Mental Health, The Sixth Hospital, Peking University <https://orcid.org/0000-0003-0376-9037>

**Cheng Zhang**

Peking University First Hospital

**Sheng He**

Institute of Biophysics, Chinese Academy of Sciences

**Ruquan Han**

Beijing Tiantan Hospital, Capital Medical University, Beijing, China

**Xiaoqun Wang**

Beijing Normal University <https://orcid.org/0000-0003-3440-2617>

**Bing Liu** (✉ [bing.liu@bnu.edu.cn](mailto:bing.liu@bnu.edu.cn))

Beijing Normal University <https://orcid.org/0000-0003-2029-5187>

---

## Article

### Keywords:

**Posted Date:** June 22nd, 2022

**DOI:** <https://doi.org/10.21203/rs.3.rs-1750692/v1>

**License:**  This work is licensed under a Creative Commons Attribution 4.0 International License.

[Read Full License](#)

---

# Hierarchical Fluctuation Shapes a Dynamic Flow Linked to States of Consciousness

Ang Li<sup>#\*1</sup>, Haiyang Liu<sup>#2,3</sup>, Xu Lei<sup>#4,5</sup>, Yini He<sup>6</sup>, Qian Wu<sup>6,7</sup>, Yan Yan<sup>8</sup>, Xin Zhou<sup>6</sup>, Xiaohan Tian<sup>6</sup>, Yingjie Peng<sup>1</sup>, Hao Yan<sup>9,10</sup>, Cheng Zhang<sup>11</sup>, Sheng He<sup>1,12</sup>, Ruquan Han<sup>\*2</sup>, Xiaoqun Wang<sup>\*6,7</sup>, Bing Liu<sup>\*6,7,13</sup>

1. State Key Lab of Brain and Cognitive Science, Institute of Biophysics, Chinese Academy of Sciences, Beijing, China

2. Department of Anesthesiology, Beijing Tiantan Hospital, Capital Medical University, Beijing China

3. Department of Anesthesiology, Qinghai Provincial Traffic Hospital, Xining, China

4. Faculty of Psychology, Southwest University, Chongqing, China

5. Key Laboratory of Cognition and Personality, Ministry of Education, Chongqing, China

6. State Key Laboratory of Cognitive Neuroscience and Learning, Beijing Normal University, Beijing, China

7. IDG/McGovern Institute for Brain Research, Beijing Normal University, Beijing, China

8. Shenzhen Institutes of Advanced Technology, Chinese Academy of Sciences, Shenzhen, Guangdong, China

9. Peking University Sixth Hospital/Institute of Mental Health, Beijing, China

10. NHC Key Laboratory of Mental Health (Peking University), National Clinical Research Center for Mental Disorders (Peking University Sixth Hospital), Beijing, China

11. The Department of Respiratory and Critical Care Medicine, Peking University First Hospital, Beijing, China

12. University of Chinese Academy of Sciences, Beijing, China

13. Chinese Institute for Brain Research, Beijing, China

**# These authors contributed equally to this work.**

**\* Correspondence to: Bing Liu (bing.liu@bnu.edu.cn), Xiaoqun Wang (xiaoqunwang@ibp.ac.cn), and Ang Li (al@ibp.ac.cn)**

# Abstract

Consciousness emerges from the spatiotemporal dynamics of neural activity. However, how such an extraordinary phenomenon is supported by neural flexibility and regional specialization across the cerebral cortex remains elusive. Here, using several functional magnetic resonance imaging (fMRI) paradigms (e.g., anesthesia, sleep, and drowsiness), we show a consciousness-related signature characterized by shifting spontaneous fluctuations along a unimodal-transmodal cortical organizational axis. The signature is simple and sensitive to altered states of consciousness in single individuals, exhibiting abnormal elevation under psychedelics as well as in individuals with psychosis. Under task-free conditions, this hierarchical dynamic reflects ongoing brain state changes in global integration and connectome diversity. Applying quasi-periodic pattern detection during different vigilance states, we found that hierarchical heterogeneity also manifested as spatiotemporally propagation waves related to arousal. A similar pattern was observed in neural activity measured with cortex-wide electrocorticography (ECoG) in macaques. Last, we observed that the spatial distribution of the principle cortical gradient not only preferentially recapitulated the genetic transcription levels of the histaminergic system but also that of the functional connectome mapping of the tuberomammillary nucleus (TMN), which promotes wakefulness. Combining behavioral, neuroimaging, electrophysiological, and transcriptomic evidence, we suggest that global state of consciousness is supported by efficient hierarchical processing that can be constrained along a low-dimensional macroscale gradient.

# Main

The stream of consciousness, as delineated by William James, is an ever-flowing mental continuity of subjective experiences. A conscious brain is capable of adapting, learning, and guiding for future actions in a constantly evolving environment. During natural sleep or pharmacological anesthesia, the consciousness entity seems to be attenuated; under psychedelics or psychosis, distortions can occur.

What is the hidden link between mental phenomena and the neural substrates of consciousness? The spatiotemporal dynamics of the brain may underlie a ‘common currency’<sup>1,2</sup>. The brain at rest is metabolically active and generates time- and space-structured spontaneous activity<sup>3</sup>, which can reflect between-subject differences in task-evoked responses, cognitive function, personality, and mental disorders. From a Bayesian perspective<sup>4,5</sup>, spontaneous brain activity sustains the top-down dynamics of predictive models to interact with sensory processing and shape perception. Accordingly, breakdowns in consciousness (e.g., during anesthesia and sleep) are accompanied by complicated changes in various aspects of the intrinsic functional organization, such as long-distance interactions<sup>6-8</sup>, anti-correlated structures<sup>9</sup>, and patterns of brain coordination<sup>10,11</sup>. Evoked spatiotemporal complexity in response to external stimulation is confined<sup>12</sup>, and functional networks degenerate as they approach the anatomical connectome backbone<sup>13</sup>. Undoubtedly, both temporal and spatial aspects of the brain’s spontaneous activity are relevant to the support of consciousness.

Temporal variability/flexibility, which is linked to the adaptability of neural systems<sup>14-16</sup>, is increasingly recognized as a key characteristic of spontaneous brain activity that can account for inter-individual age- and performance-related traits. Computational models indicate that such slow, scale-free dynamics enable the criticality and metastability of non-linear systems, thus supporting a broader repertoire of brain states and transitions<sup>15,17-19</sup>; Conversely, task-evoked activity increases stability and quenches signal variability<sup>20,21</sup>. In the spatial domain, resting-state BOLD variability recapitulates the relative expression of cell markers for input-modulating somatostatin and output-modulating parvalbumin interneurons<sup>22</sup>. The local density of these two interneurons is linked to the balance between inhibitory control and cortico-cortical communication<sup>23</sup>. In light of the above, we speculated that a topographically organized neural variability pattern may orchestrate the rise and fall in global states of consciousness. Importantly, this hypothesis caused us to emphasize a search for temporal-spatial nested signature rather than a specific temporal feature or location.

To test this, we incorporated several different fMRI paradigms capturing dynamic states of consciousness, from deep sleep or under anesthesia to alert wakefulness. First, we systematically investigated how spatiotemporally embedded variability across the neocortex changes in three conditions -- dexmedetomidine-induced sedation, normal sleep, and resting-state scanning, in which a proportion of individuals tend to be naturally drowsy in minutes. The results revealed a common hierarchical shift in cortical spontaneous activities. Second, to validate the signature, we collapsed the spatiotemporal dynamics into a simple, low-dimensional index to delineate the hierarchical fluctuation on the level of minutes. The hierarchical index was further tested for different energetic states (i.e., caffeine or fasting) of a single densely sampled person, volunteers who had been administered a psychedelic drug, and individuals with neuropsychiatric disorders.

1 Subsequently, based on fMRI data from the Human Connectome Project (HCP), we revealed that the hierarchical fluctuation  
2 covaried with the global integration topology, connectome complexity, and an infra-slow propagation wave previously  
3 found to pertain to arousal modulation. Similar hierarchical signatures can also be observed in macaques based on ECoG  
4 recordings. Furthermore, a spatial analysis using the genetic transcriptome from the Allen Human Brain Atlas and HCP 7T  
5 high-resolution fMRI data implicated a contribution of the hypothalamic TMN region, which regulates wakefulness. Lastly,  
6 a hypothetical model was proposed to explain all our observations.

## 8 **Results**

### 10 **Hierarchical Cortex-wide Fluctuations Reflect Ongoing States of Consciousness**

12 Neural variability, which was operationalized as the standard deviation of low-frequency BOLD signal for each voxel/vertex  
13 across time, yielded a similar pattern to that found using frequency-based measurements (e.g., fractional amplitude of low-  
14 frequency fluctuation<sup>24</sup>, Supplementary Fig.1, Methods). The cortical map was further *z*-normalized to highlight the spatial  
15 heterogeneity of temporal fluctuations. To determine whether there is a shared consciousness-related pattern of shifts, we  
16 analyzed group-level shifts in cortical activity across three fMRI paradigms (Datasets 1-3). In Dataset 1 (Fig. 1a; Methods),  
17 we compared 21 healthy volunteers across three conscious states: wakefulness, dexmedetomidine-induced sedation, and  
18 recovery (paired *t*-statistic contrast shown in Fig. 1b and Supplementary Fig 2). Dataset 2 comprised the resting state fMRI  
19 data from a large sample of healthy subjects from the HCP project. For each person, we segmented each run of four into  
20 non-overlapping ~36 s time fragments (50 frames) and regarded their sequence as a coarse proxy of vigilance information,  
21 which generated up to millions of dense state pairings. The correlation between the normalized signal amplitude and the  
22 temporal distance between two segments can be approximately defined as the effects caused by a drop in alertness across  
23 14.4 minutes (Fig. 1d-e, Methods). In Dataset 3, we analyzed simultaneous EEG-fMRI data from 6 healthy volunteers during  
24 2 hours of sleep, to investigate alterations in the low-frequency BOLD variability pattern (Fig. 1g-h) that accompanies  
25 manually labelled sleep stages (i.e., N1, N2 and slow-wave sleep, Methods). We observed a consistent pattern across these  
26 three experiments (Fig.1j), suggesting that there is a cortex-wide consciousness-specific signature. This pattern spatially  
27 recapitulated a large-scale cortical hierarchy, indicating that the allocation of neural variability continuously shifts from the  
28 association areas<sup>25</sup> (Fig. 1h-l, default mode, control, and limbic networks) to low-level sensory cortices (Fig. 1h-l, visual  
29 and sensorimotor networks) with waning consciousness. Quantitatively, this pattern was highly correlated with the principle  
30 functional gradient calculated from dense functional connectome data (Fig. 1c, f, i), as well as with intracortical myelination  
31 based on T1-/T2-weighted ratio maps (Supplementary Fig.3). These correlations were not simply driven by contrasts across  
32 large chunks of regions but were also observed within most single functional networks (Supplementary Fig. 3).

### 34 **Characterizing Hierarchical Dynamics in Single Individuals**

36 To characterize the above signature at the individual level, we collapsed the cortical neural variability into a simplified low-  
37 dimensional representation, naming it the ‘hierarchical index’. Practically, we defined the index as the rank correlation

1 coefficient between the spatial distribution of cortical BOLD variability and the group-level principle functional gradient  
2 (Methods). Such a hierarchical index can provide a proxy for the way that low-frequency activities distribute along the  
3 cortex-wide hierarchical axis. In Dataset 1, we found that the hierarchical index could clearly distinguish three conscious  
4 states, showing a reduction in 20 of 21 participants from wakefulness to sedation (Fig. 2a). In Dataset 2, the hierarchical  
5 index significantly decreased across the fMRI scanning in 37.4% of the individual runs, but only 1.1% significantly  
6 increased (Fig. 2b,  $P < .05$ ). Interestingly, after performing partial correlations controlling for sex, age, and head motion,  
7 the average index across the four runs significantly associated with inter-individual differences relating to vigilance, such  
8 as in sleep quantity, impulsivity, response time, and accuracy during task fMRI (Fig. 2b, Methods, Supplementary Table 1).  
9 In Dataset 3, the hierarchical index was able to sensitively track all 6 individuals' sleep stages, as manually labelled by  
10 experts (Fig. 2c,  $r = 0.75-0.89$ ,  $P_s < .0001$ ). To further characterize the dynamics of the signature over a much longer  
11 timescale, we used a longitudinal resting-state fMRI dataset of a heavily sampled individual from the MyConnectome  
12 Project<sup>26</sup> (Dataset 4, Methods). As expected, the hierarchical indexes in the fed/caffeinated state (on Thursdays) were  
13 considerably higher than those in the fasted/uncaffeinated state (on Tuesdays), enabling a univariate classification accuracy  
14 over 80% (Fig. 2d, Mann–Whitney u test;  $P < .0001$ ). The hierarchical index also associated with daily fluctuations in  
15 fatigue (Fig. 2e,  $r = -0.48$ ,  $P < .0001$ ) and heightened attention (Fig. 2f,  $r = 0.49$ ,  $P < .0001$ ) based on the self-reported  
16 Positive and Negative Affect Schedule (Methods). The above results demonstrate that the hierarchical dynamics of cortical  
17 variability could capture shifts in conscious states within a single person over minutes, hours, and days, and across  
18 individuals.

## 19 20 **Hierarchical Dynamics in Psychedelic and Psychotic Brains**

21  
22 Previous work indicated that psychedelic or psychotic states can be considered to be ‘higher’ or ‘abnormal’ states of  
23 consciousness<sup>27–29</sup>. Therefore, we next employed an openly available Dataset 5 (Methods) that included 15 healthy subjects  
24 who were administered both LSD and placebo<sup>30</sup>. Interestingly, using between-session testing, we found that the hierarchical  
25 indexes were significantly higher in the LSD condition than in the placebo (Fig. 3a,  $P < .0001$ ). Furthermore, using the  
26 Neuropsychiatric Phenomics Consortium data<sup>31</sup> (Dataset 6, Methods), we showed that the hierarchical index was  
27 significantly associated with inter-individual psychotic symptoms, particularly those symptoms which can be induced by  
28 psychedelics (such as hallucinations, Fig. 3b). Correspondingly, hierarchical disturbances were also observed during the  
29 resting-state in individuals with schizophrenia and bipolar disorder (Fig. 3c), but not in those with attention  
30 deficit/hyperactivity disorder. The effect can be replicated in a cross-ethnic cohort that included individuals with  
31 schizophrenia (Dataset 6). These results suggest that the hierarchical signature relating to states of consciousness can also  
32 capture considerable effects in both people using psychedelics and in those with neuropsychiatric disorders, but the  
33 disturbances occur in the opposite direction compared with sleep or anesthesia.

## 34 35 36 **Complex Brain Integration and Differentiation**

1 Multiple theories<sup>32</sup> suggest that conscious experiences require both functional integration (impossible to decompose) as well  
2 as diversity (richness and unpredictability of information). In light of these earlier theories, it is possible that hierarchical  
3 dynamics would support a flexible connectome reconfiguration in cortical integration and diversity during the resting state.  
4 Thus, we calculated the global signal (GS) topology to form a spatial map measuring how different regions entrained the  
5 average fluctuation to characterize global integration across the neocortex (Fig. 4a). Previous work revealed the spatial  
6 structure and behavioural relevance of GS topology<sup>33,34</sup>, but few considered its temporal reconfiguration during task-free  
7 states. Here, we used a data-driven approach to cluster time-resolved GS topologies into concatenated GS maps for 100  
8 unrelated participants from the HCP (replication in another 100 independent subjects, Supplementary Fig. 4). We found that  
9 the hierarchical index can well explain the distinct patterns of the GS topology: higher indexes corresponded to a GS  
10 topology that spatially resembled the cortical hierarchy (Fig. 4b,  $r = 0.59$ ,  $P < .0001$ ); two variables substantially  
11 summarized the 2-cluster solution of GS topologies by K-means (Methods). The GS topology difference between two states  
12 was highly analogous to the cortical hierarchy (Fig. 4e,  $r = 0.89$ , State 1: higher hierarchical index and global signals are  
13 more ‘integrated’ by associated regions; State 2: opposite). Note that these clustering experiments were not designed to  
14 discover the optimal dispersed states but to capture primary temporal heterogeneity. The graph theory approach was also  
15 utilized and yielded similar results (by defining nodewise integration as the sum of functional connectivity, Methods,  
16 Supplementary Fig. 5). We also calculated the connectome and temporal entropy for time-resolved brain states (Fig. 4c,  
17 Methods). Both measures, especially connectome entropy, were considerably higher during the periods of State 1 compared  
18 with State 2 (Fig. 4d, 4f).

19  
20 The results indicated that during resting states with a high hierarchical index, cortical activity more likely exhibited a  
21 complicated integrated pattern, which was different from the ‘GS topology stereotype’ dominated by the sensory cortices,  
22 achieving elevated functional diversity in the connectome and in temporal fluctuation, which may support cognitive  
23 demands during high vigilance. In this section and the following one, resting-state fMRI data from the HCP dataset was  
24 analyzed while considering: i) its high signal:noise ratio, temporal resolution, and large sample size; and ii) that it can reveal  
25 rich dynamics in global conscious states, ranging from vivid waking states to natural light sleep<sup>35</sup>.

## 26 27 **Relationship to the Infra-Slow Cortex-wide Propagation Phenomenon**

28  
29 Hierarchical dynamics may relate to infra-slow arousal regulation. In human fMRI studies, recent work has consistently  
30 revealed an infra-slow global wave<sup>36-38</sup> that intrinsically propagates along the macroscale functional gradients (i.e., from  
31 the somatomotor and higher-order visual areas toward the control and default mode networks) and that is relevant to arousal  
32 and autonomic fluctuations. Based on a data-driven quasi-periodic pattern (QPP) analysis<sup>37</sup>, a stereotyped wave lasts  
33 approximately 20 seconds and can explain the most primary recurring spatiotemporal pattern in resting-state fMRI. A similar  
34 wave of gamma activity can be observed from ECoG data as part of an arousal-related sequential spectral transition (SST)  
35 event<sup>39</sup>, which correlates with a global fMRI peak and with a decrease in arousal<sup>40</sup> (relevant analysis in the next section). It  
36 is still unknown whether temporal heterogeneity exists in the infra-slow global wave across different states of vigilance.  
37 Based on our results, we speculate that during higher states of vigilance, such a spatiotemporal wave would more likely

1 ‘propagate’ to the association cortex to modulate excitability and thus complete an unabridged QPP cycle (e.g., anti-  
2 correlation pattern in fMRI).

3  
4 Thus, we analyzed the resting-state fMRI data from the 100 participants in the HCP who showed the greatest reduction in  
5 the hierarchical index across four runs (average Pearson’s  $r < -0.49$ , Methods) and truncated their initial and terminal 400  
6 frames as coarse proxies for the high and low vigilance states, respectively. To determine the typical global wave, we  
7 downloaded a recently published QPP template<sup>37</sup>, which was calculated from HCP resting-state fMRI data using a  
8 computationally expensive algorithm (only cortical regions were included). The framewise propagation pattern can be seen  
9 in Fig.5 based on its distribution along the functional gradient. We applied the sliding-window approach to detect QPP  
10 events across two different states (Fig 5a-b; Methods; threshold  $r = 0.4$ ; initial states: 789 events, terminal states: 1000  
11 events). To acquire representative dynamics, we extracted the average time series from the top and bottom 20% cortical  
12 hierarchy regions with QPP events. We found that almost all low-order fluctuations exhibited similar dynamics, resembling  
13 the typical trajectory in the group template (Fig 5c, e). However, the high-order fluctuations bifurcated into distinct modes  
14 (Fig 5d): typical trajectories (Fig 5f: left; ‘high vigilance’) or atypical trajectories (Fig 5f: right, ‘low vigilance’). In  
15 accordance with our hypothesis, the great majority of trajectories were ‘typical’ in the initial 400 frames (i.e., were more  
16 likely with higher vigilance). The proportion of ‘atypical’ trajectories significantly increased during the terminal 400 frames,  
17 indicating that such waves were more likely to be disregarded in the regulation of higher networks. Meanwhile, the lower-  
18 order regions had larger fluctuations and thus dominated the global signal. With regard to functional connectivity within the  
19 QPP events, the initial periods exhibited more anti-correlation structures between the internal (default mode and control  
20 networks) and external systems (attention and sensory networks) and were greatly diminished by the end of the scanning  
21 session. This anticorrelation structure was previously considered to be a signature for the waking state in comparison with  
22 anesthesia<sup>13</sup> or disorders of consciousness<sup>41</sup>. In summary, our work suggested significant heterogeneity in the infra-slow  
23 wave primarily in the higher-order areas across different brain states. A hypothetical model is provided in our Discussion  
24 below.

## 25 26 **Hierarchical Dynamics in Macaque Electroencephalography**

27  
28 BOLD signal fluctuation reflects localized changes in neural activity indirectly through a complex neurovascular coupling.  
29 We ascribed the observed hierarchical signature to altered neuronal activity rather than to the physiological baseline.  
30 Previous experimental studies<sup>42,43</sup> suggested that local field potential gamma power (nominally 40-100 Hz) could serve as  
31 a mediator, closely coupling the infra-slow BOLD fluctuations to the localized coordination of neural activities. We  
32 speculate that variability in the gamma band-limited power (BLP) may reflect a similar hierarchical shift during altered  
33 states of consciousness.

34  
35 We tested this idea using openly available data from the Neurotycho project<sup>44,45</sup> (Dataset 7). Specifically, we accessed the  
36 spontaneous cortical activity from large-scale, spatially resolved electrophysiological recordings in two densely sampled  
37 macaques across the awake, sleeping, and anesthetized states. Accordingly, a diffusion embedding algorithm was applied

1 to 128-channel functional connectome data obtained by gamma-BLP. Consistent with a recent work<sup>36</sup>, the principal gradient  
2 could be identified in each macaque, recapitulating the unimodal-transmodal hierarchy across the neocortex (Fig. 6 a-b).  
3 Following the analysis pipeline for the human fMRI data, we compared the normalized, moment-to-moment fluctuations in  
4 gamma-BLP across distinct states of consciousness using equivalent, segmented time windows (150 seconds, Methods).  
5 Similarly, in comparison with the awake states, the patterns of neural variability varied significantly along the macroscale  
6 hierarchy during sleep and anesthesia (Fig. 6 c-f, *Chibi*:  $r_{\text{awake vs sleep}} = 0.61$ ,  $r_{\text{recovery vs anesthesia}} = 0.55$ ; *George*:  $r_{\text{awake vs sleep}} =$   
7  $0.84$ ,  $r_{\text{recovery vs anesthesia}} = 0.63$ ). These hierarchical shifts in both the electrophysiological and BOLD signals imply a common  
8 consciousness-related signature of cortical activity (gamma-band hierarchical index shown in Fig. 6 g-h).  
9

10 Next, we performed a QPP analysis on the macroscale, cortex-wide gamma-BLP fluctuations. A propagating wave that was  
11 analogous to that found using human fMRI data was revealed (Fig. 6 i-j, Methods). Meanwhile, the average spectrogram of  
12 the gamma-BLP QPP events comprised the loss of mid-frequency activity as well as concurrent increases in low-frequency  
13 power and resembled a pattern of sequential spectral transitions (SSTs, as shown in Fig. 6 k-l and Supplementary Fig. 6).  
14 As mentioned above, SST events were identified by momentarily increases in delta power and are suggested to be involved  
15 in arousal modulation. Specifically, the resemblance between the gamma-BLP QPP and the SST average patterns is more  
16 evident during eye-closed and sleeping conditions (Supplementary Fig. 6) when the SST pattern was reported to be more  
17 stereotypical<sup>39</sup>. When considered alongside a recent work that revealed the gamma component of SSTs to be a traveling  
18 wave<sup>36</sup>, it seems that enhanced cortical excitability and the emergence of slow oscillations tend to couple together, resulting  
19 in the gamma and delta components in both the gamma-BLP QPP and SST. Unlike the anti-correlation in the fMRI QPP  
20 pattern<sup>37</sup>, the average gamma-BLP signals of low- and high-order regions (top and bottom 20 channels based on the principle  
21 embedding) primarily increased in the first half (Fig. 6 k-l) and had shorter time delays between their peaks (*Chibi*:  $\sim 2.4$  s;  
22 *George*:  $\sim 0.8$  s). Using the peak difference between the low- and high-order regions, we observed that a relatively larger  
23 gamma BLP tended to emerge in the high-order cortex during higher levels of consciousness (Fig. 6m; Methods; Monkey  
24 *Chibi*: eye-opened > eye-closed:  $t = 8.9$ ,  $P < .0001$ , eye-closed > sleep:  $t = 5.0$ ,  $P < .0001$ ; Monkey *George*: eye-opened >  
25 eye-closed:  $t = 5.5$ ,  $P < .0001$ , eye-closed > sleep:  $t = 2.3$ ,  $P < .019$ ; paired  $t$ -test). Remarkably, this peak difference was  
26 predictive of subsequent global changes in delta power during eye-closed and sleeping conditions when SST-like patterns  
27 were evident (Methods; Fig. 6n, Monkey *Chibi*:  $r = -0.47$ ,  $P < .0001$  at eye-closed condition,  $r = -0.43$ ,  $P < .0001$  during  
28 sleeping; Monkey *George*:  $r = -0.45$ ,  $P < .0001$  at eye-closed condition,  $r = -0.37$ ,  $P < .0001$  during sleeping). These  
29 preliminary results indicate a heterogeneous regulation of the gamma-BLP wave in distinct states of consciousness,  
30 emphasizing the excitability along the cortical hierarchy: a higher gamma BLP propagating (from the unimodal) to the high-  
31 order cortex is associated with the subsequent emergence or suppression of cortical slow oscillations.  
32

### 33 **Implication of Histaminergic System**

34  
35 The action of the ascending reticular activating system (ARAS) on the cerebral cortex is essential for maintaining  
36 consciousness and involves complex interactions between multiple neurotransmitters. Specific subsystems in the ARAS  
37 may preferentially underpin the hierarchical dynamics across the neocortex, which could show spatial similarity between

1 the genetic expression patterns of molecular markers and the cortical functional gradient. Therefore, we next conducted a  
2 cross-modal analysis to search for genetic transcriptomes that were unimodally-transmodally distributed based on the Allen  
3 Human Brain Atlas (Methods).

4  
5 Interestingly, after identifying the top associated genes (Supplementary Table 2), we found that the *HDC* (histidine  
6 decarboxylase, which is the unique enzyme catalysing the decarboxylation of histidine to form histamine) gene was one of  
7 the most prominent genes (Fig. 7 a, b, d, ranked 3rd among 20,737 genes involved). The leading position of the *HDC* gene  
8 was well replicated using another two independent analysis pipelines (Supplementary Table 3): i) It ranked 5<sup>th</sup> based on the  
9 resource released by Anderson and colleagues<sup>22</sup>. And ii) it showed the 9<sup>th</sup> largest variance in the online open-science  
10 Neurovault platform (Supplementary Table 4). Moreover, the spatial distributions of the expressions of the *HDC* and *HRH1*  
11 (Histamine Receptor H1, administration of histamine or H1 receptor agonists can induce wakefulness) genes are highly  
12 correlated (Fig. 7c,  $P < .0001$ ). The tuberomammillary nucleus (TMN) in the posterior hypothalamus, as a wake-promoting  
13 centre, is the primary source of brain histamine and widely projects histaminergic neurons to the cerebral cortex. Given the  
14 above results, we speculated that the expressions of the *HDC* gene should be non-randomly and elaborately distributed  
15 across the cerebral cortex, possibly recapitulating the densities of histaminergic projections. We next applied a recently  
16 developed hypothalamus atlas<sup>46</sup> and high-resolution 7T resting-state fMRI data from the HCP (Dataset 8) to examine  
17 whether functional connectivity between the TMN and the cortical regions would exhibit similar spatial patterns (although  
18 BOLD signals showed a narrow dynamic range in the hypothalamus). The result was that the TMN showed the most  
19 significant correlations with the functional gradient (Fig. 7e) across 13 hypothalamic regions. These evidences from both  
20 transcriptome and functional connectome data suggest a role of the histaminergic system in modulating the hierarchical  
21 dynamics across the neocortex.

## 22 23 24 25 **Discussion**

26  
27 In the present work, integrating different experiment paradigms (i.e., sleep, anesthesia, drowsiness, psychedelia, and  
28 psychiatric disorders), designs (intra- and inter-subject variability), timescales (ranging from several minutes to years),  
29 imaging modalities, and species, we revealed a simple phenomenon: A hierarchical shift in cortical neural variability was  
30 linked to global states of consciousness. Furthermore, we extended the hierarchical heterogeneity to the time-resolved  
31 connectome reconfiguration, an arousal-related traveling wave, and a specific wake-promoting system. In the following  
32 discussion, we will summarize a hypothetical model that can account for these findings (Fig. 8). In brief, we propose that  
33 global consciousness depends on the global availability of hierarchical processing, which manifests as disproportional  
34 fluctuations within the association cortices. During vivid wakefulness, the hierarchical heterogeneity is modulated by  
35 spatiotemporal waves of excitability and by the histaminergic arousal system, enabling complex patterns of functional  
36 integration and diversity. A detailed mechanism for the hypothetical model awaits future investigation.

## 1 A Hypothetical Model Pertaining to Theories of Consciousness

2  
3 We speculate that variations in the fluctuations along a unimodal-transmodal axis (Fig.8 a-b) reflect a large-scale breakdown  
4 in hierarchical information processing, in particular in top-down modulation. Increasing evidence suggests that top-down  
5 dynamics act as generative models and interact with sensory processing along a macroscopic cortical hierarchy<sup>47</sup>. Top-down  
6 processing is emphasized in major theories of consciousness, and perturbations of this processing are involved in the  
7 pathogenesis of coma<sup>48</sup> and psychosis<sup>49</sup>. In integrated information theory (IIT), complex systems were predicted to be  
8 “zombies” in the absence of a feedback mechanism<sup>50</sup>. Accordingly, global neuronal workspace theory<sup>51</sup> (GNW) predicts a  
9 set of distributed excitatory (workspace) neurons, which intrinsically situate in higher hierarchies to receive bottom-up  
10 information and can flexibly mobilize or suppress local processors through descending projections. We suggest that these  
11 workspace neurons overwhelmingly distribute across heterogeneous, higher-order networks. GNW also predicts that  
12 stochastic spontaneous “ignitions” can provide a source of diversity that continuously activates mental representations at  
13 rest. These may explain our observations that, during a state of high vigilance, associative areas exhibited larger fluctuations  
14 and simultaneously tended to be the integrative center that maximized functional complexity. The temporal correlation with  
15 large-scale brain dynamics also accords with the concept of the dynamic core hypothesis, which highlights both neural  
16 integration and complexity as supporting consciousness. Interestingly, after summarizing previous fMRI studies that tried  
17 to localize a consciousness-specific region, we found that most of the reported regions were distributed in areas with extreme  
18 gradients, regardless of their anatomical nonconvergence (Supplementary Table 5). For example, He et al. reported that  
19 low-frequency BOLD activity increased in external networks and decreased in internal networks in disorders of  
20 consciousness<sup>52</sup>.

21  
22 Our results provided new insights into the relationship between the global states of consciousness and global waves. This  
23 part of the analysis was built on recent studies that unified spatiotemporally recurring waves<sup>36,37,39</sup> observed in BOLD and  
24 gamma BLP signals as an intrinsic physiological process linked to arousal. The topographically organized patterns of  
25 excitability temporally correspond to arousal fluctuations and influence sensory processing. Extending previous findings,  
26 we demonstrated the infra-slow propagation wave as a heterogeneous event relating to current brain states. Specifically,  
27 during high vigilance, the waves were more spatiotemporally stereotypical. In contrast, even in the presence of larger  
28 fluctuations that started in the sensory cortices, the propagation appeared to be interrupted in the higher-order regions. We  
29 thus propose that such slow, autonomic processing stabilizes wakefulness mainly by modulating the neuronal excitability  
30 of the higher-order association cortices. The failure of this modulation may facilitate the transition toward unconsciousness  
31 and promote slow oscillations relating to sleep and memory consolidation. Our model predicts that the global coordination  
32 activity bifurcates into a typical mode (i.e., anti-correlation organization) and an atypical mode (i.e., increased delta power  
33 in SSTs) depending on the higher-order networks. This accords with several previous observations, such as larger sensory-  
34 dominant fluctuations (dominating global signal) during drowsiness<sup>53-55</sup> and elevated activity of default mode areas  
35 preceding pupil dilation<sup>56</sup>. A recent work<sup>57</sup> identified considerable negative- and positive-delay neurons in immobilized  
36 mice and studied the sequential activation that was related to pupil diameter, delta power, and hippocampal ripples.

1 Our work suggested a hierarchical organization of the histaminergic system across the neocortex. Histamine plays a  
2 prominent role in maintaining wakefulness<sup>58</sup> through projections into widespread cortical and subcortical regions. TMN  
3 neurons, the only source of histamine in the central nervous system, fired fastest during the high vigilance state, showed  
4 reduced activity in quiet wakefulness, and were quenched after falling sleep. A recent study found that hypothalamic TMN  
5 can broadcast dual inhibitory-excitatory signals throughout the neocortex through GABA-histamine axons<sup>59</sup>. The balance  
6 between the two components may regulate the neural dynamic range and control the degree of wakefulness. Administration  
7 of antihistamines (H1 receptor antagonist) commonly induces drowsiness not only in mammals but also in flies and zebrafish.  
8 Because of the spatial overlap between low-dimensional functional embedding, histaminergic molecular signatures, and the  
9 TMN functional connectome that we identified, we suggest that the neocortical regions receive axonal projections from the  
10 TMN neurons along a macroscale gradient. The histaminergic system potentially interacts with other ARAS subcortical  
11 nuclei (such as in the forebrain, which is a potential source of the global signal<sup>60</sup>) to generally support cortical hierarchical  
12 dynamics.

### 13 14 **Significance of the Hierarchical Organization**

15  
16  
17 The principal gradient of dense functional connectome and T1w/T2w ratio maps, which are highly correlated ( $r = -0.76$ ),  
18 were utilized as surrogates of cortical hierarchy. Both had a fine resolution and had previously been shown to be coupled  
19 with the anatomy of the hierarchy, such as defined by feedforward and feedback projections<sup>61</sup>. To reflect hierarchical  
20 organization in the functional domain, the principal gradient map was chosen in our main analyses. Interestingly, the cortex-  
21 wide map releveling in the sleep experiment showed higher spatial similarity with the T1w/T2w pattern, suggesting that the  
22 signature shifts to a structural skeleton during deeper unconscious states. A recent fMRI study characterized a hierarchical  
23 signature based on transfer entropy (measuring information flow), which yields a similar macroscale pattern<sup>62</sup>. Unlike the  
24 abovementioned anatomically or functionally defined hierarchies, a recent whole-brain computational modelling study<sup>63</sup>  
25 reported an altered diversity of ‘intrinsic ignition’ (capability of a region to propagate neuronal activity) induced by  
26 anesthesia as an indicator of hierarchical disruption.

27  
28 The default-mode network (DMN) is located on the top of the principal gradient. Although traditionally viewed as a task-  
29 negative network, the DMN is active when making social or self-referential inferences and was recently suggested as  
30 carrying rich information related to conscious perception even during BOLD deactivation<sup>64-66</sup>. As a conservative system, it  
31 is possible that histaminergic regulation of wakefulness evolutionally developed along this hierarchical axis, which also  
32 captures dominant variations in synaptic excitation and inhibition<sup>67</sup>, the intrinsic timescale<sup>67</sup>, and gene expression, to  
33 optimize hierarchical information processing for advanced cognition.

34  
35 Such a hierarchical architecture and dynamics would also be critical for an intelligence system. Sleep, as a physiological  
36 cycle in which vigilance is thoroughly lost, seems deleterious for survival but is prevalent in living animals. Converging  
37 evidence shows that sleep, even a short nap, can substantially inspire novel problem solving<sup>68</sup>. The recently proposed  
38 overfitted brain hypothesis<sup>69</sup> suggested that a dedicated offline period is useful for combatting the brain’s tendency to overfit

1 in daily learning. In comparison with deep learning, this theory suggests that the dropout technique can prevent overfitting  
2 by randomly ignoring neurons during training. Experimental data indicated that, to learn more abstract representations,  
3 neuron dropout could be preferentially deployed in deep layers to introduce noise; conversely, lower layers are more stable  
4 and suitable for the transfer of learning. Corresponds to our results, it is possible that neocortex conducts its ‘noise injection’  
5 in a heterogeneous manner across the hierarchical organization during state of decreased consciousness. Certainly, the  
6 human brain is far more efficient in cross-hierarchical communication than are artificial networks. This efficiency may be  
7 attributable to the rich spontaneous synchronization, embedded distributed higher-order cortices, and abundant feedback  
8 pathways.

## 10 **Global and Physiological Nuisance Signals**

12 The interpretation of the global signal is quite obscure, and its spatial contribution is structurally heterogeneous across the  
13 brain. The GS topography was shown to be aberrant in schizophrenia<sup>33</sup>, bipolar disorder<sup>70</sup>, and epilepsy<sup>71</sup>, and can be  
14 significantly modulated by external stimuli<sup>72</sup>. Applying K-means clustering on time-resolved GS topography, we suggest  
15 that the reconfiguration of the GS topography reflects a large-scale, dynamic integration linking to vigilance states during  
16 rest. Thus, the GS regression strategy may reduce such dynamical topography across time, which probably distorts state-  
17 dependent analyses<sup>73</sup> but strengthens trait-like functional representations<sup>74</sup>. Additionally, we showed that the GS regression  
18 procedure has minimal effect on the hierarchical index (Supplementary Materials). Using HCP data that included  
19 simultaneous physiological recordings, we demonstrated that regressing out the respiratory and cardiac cycles did not  
20 influence our key results (Supplementary Materials). An additional analysis was also performed to evaluate the potential  
21 effects of head motion (Methods; Supplementary Materials). Critically, our results based on macaque electrocorticography  
22 data largely mitigated the concerns potentially introduced by motion artifacts and physiological nuisance data in human  
23 fMRI results.

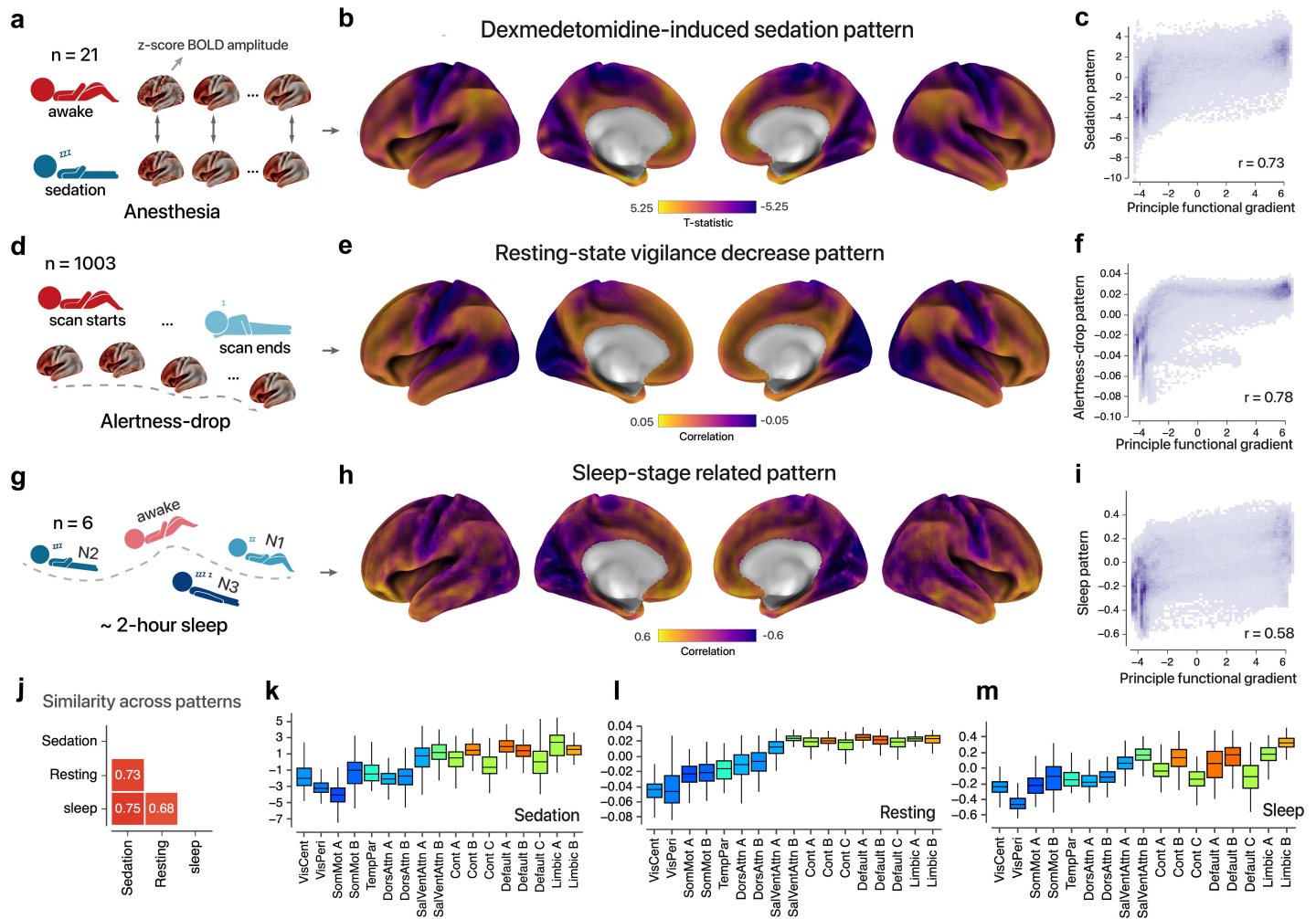
## 25 **Limitations**

27 Several limitations should be noted. First, level of consciousness is an ambiguous construct<sup>75</sup>, and our study neglected  
28 consciousness as a multidimensional phenomenon. It is also an oversimplification to attempt to unify physiological sleep,  
29 pharmacological sedation, and psychedelic states into the same framework, and mechanisms that might distinguish them  
30 were not fully investigated. Second, our time-resolved state and recurring QPP analyses were restricted to HCP fMRI data,  
31 which might introduce biases into our hypothetical explanation of other conditions. The high-resolution fMRI design should  
32 be utilized to untangle the hierarchical interaction and global traveling waves across more paradigms. Third, we did not  
33 address how choices of different MRI scanners, head coils, or acquisition parameters could systematically influence the  
34 spatial distribution of temporal noise and the hierarchical index, which could limit the potential application of cross-scanner  
35 generalization. Thus, additional normalization, acquisition methodologies, and modalities (e.g., near-infrared  
36 spectrophotometry) should be carefully tested in the future to ascertain the practical application of our findings.

1 **Conclusions**

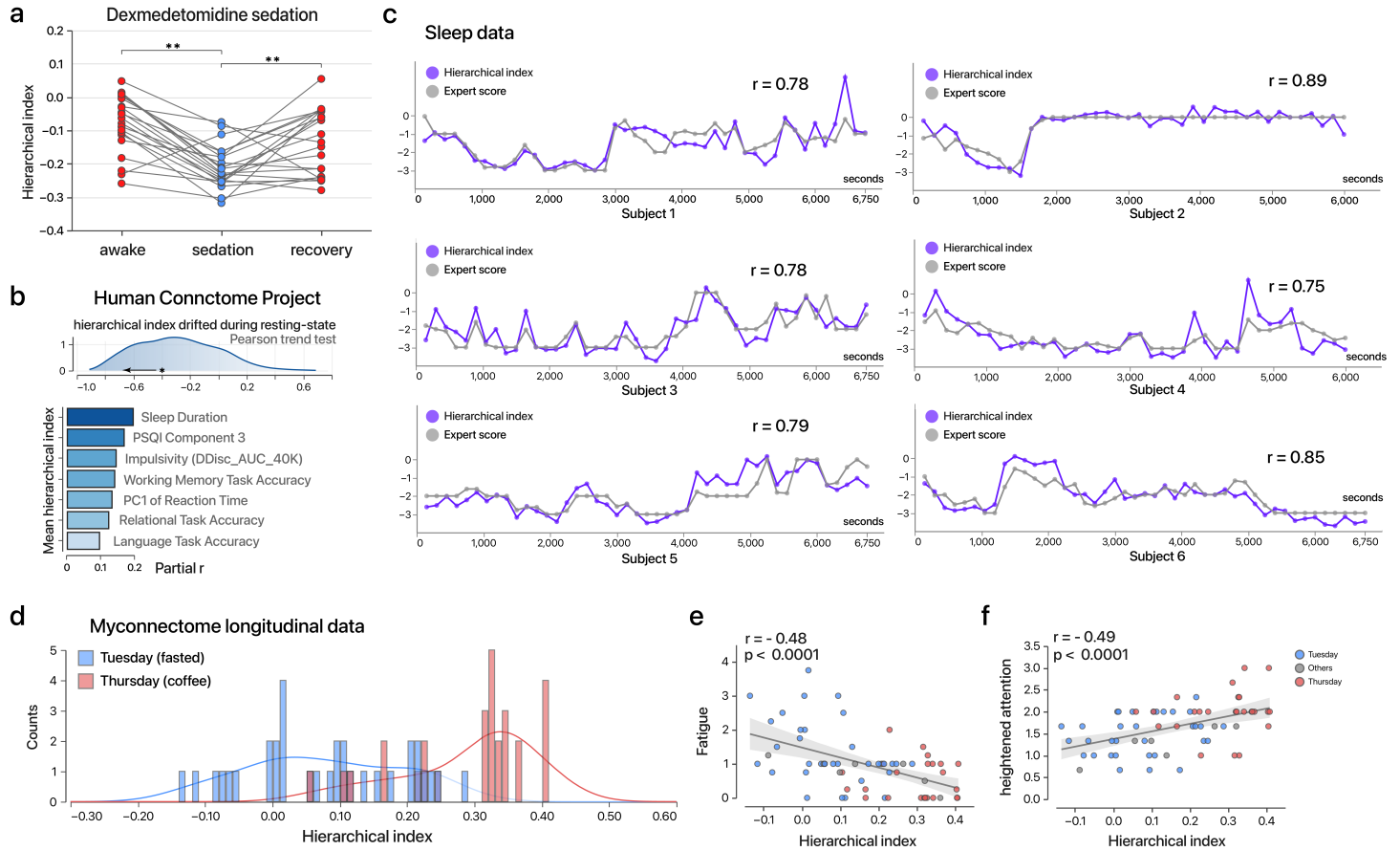
2  
3 This work suggests that human consciousness is supported by sophisticated hierarchical interactions that can be constrained  
4 along a low-dimensional macroscale gradient. Phenotypically, loss of consciousness is likely to couple with the breakdown  
5 of this processing, which is marked by spatially shifted neural activities along the cortical hierarchy.  
6  
7  
8  
9  
10  
11  
12  
13  
14  
15  
16  
17  
18  
19  
20  
21  
22  
23  
24  
25  
26  
27  
28  
29  
30  
31  
32  
33  
34  
35  
36  
37

**Fig 1. Shared spatial signature of cortex-wide BOLD amplitude relating to anesthesia, sleep, and vigilance.**



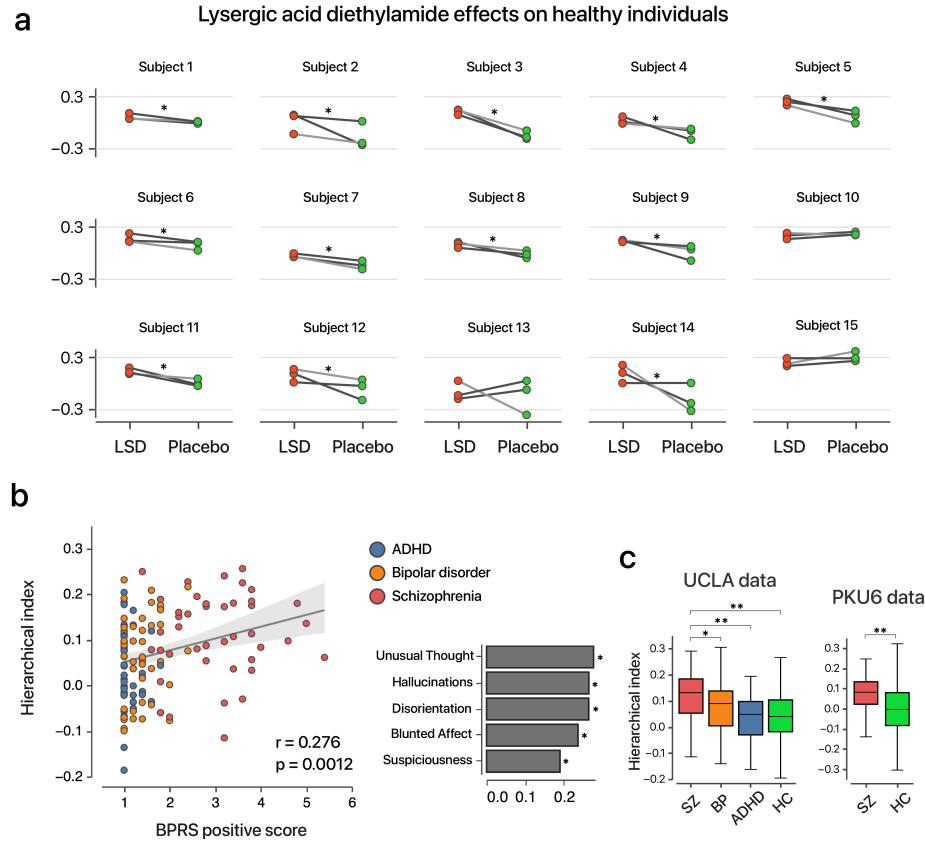
**a**, Schematic diagram of the dexmedetomidine-induced sedation paradigm; z-normalized BOLD amplitude was compared between initial wakefulness and sedation states ( $n = 21$ ) using a paired sample  $t$ -test; fMRI images were also collected during the recovery states and exhibited a highly consistent result (Supplementary Figure 2). **b**, Cortex-wide, unthresholded  $t$ -statistical map of dexmedetomidine-induced sedation effect. For the purposes of visualization as well as statistical comparison, the map was projected from the MNI volume into a surface-based CIFT1 file format and then smoothed for visualization (59412 vertexes; the same projection was utilized for the following sleep-stage map). **c**, Principle functional gradient captures spatial variation in the sedation effect across the surface area (wakefulness versus sedation:  $r = 0.73$ ,  $P < .0001$ , Spearman rank correlation). **d**, During the resting-state fMRI acquisition, the level of vigilance is hypothesized to be inversely proportional to the length of scanning in a substantial proportion of the HCP population ( $n = 982$ ). **e**, Cortex-wide unthresholded correlation map between time intervals and z-normalized BOLD amplitude; a negative correlation indicates that the signal became more variable along with scanning time and vice versa. **f**, The principle functional gradient is correlated with the vigilance decrease pattern ( $r = 0.78$ ,  $P < .0001$ , Spearman rank correlation). **g**, Six volunteers participated in a 2-hour EEG-fMRI sleep paradigm; the sleep states were manually scored into wakefulness, N1, N2, and slow-wave sleep by two experts. **h**, The cortex-wide unthresholded correlation map relating to different sleep stages; a negative correlation corresponds to a larger amplitude during deeper sleep and vice versa. **i**, The principle functional gradient is associated with the sleep-related pattern ( $r = 0.58$ ,  $P < .0001$ , Spearman rank correlation). **j**, Heatmap plot for spatial similarities across sedation, resting-state drowsiness, and sleep patterns. **k-m**, Box plots showing consciousness-related maps (b-e) in 17 Yeo cortical networks<sup>25</sup>. Box colour indicates average functional hierarchy.

**Fig 2. Low-dimensional hierarchical index tracks fluctuations in multiple consciousness-related brain states.**



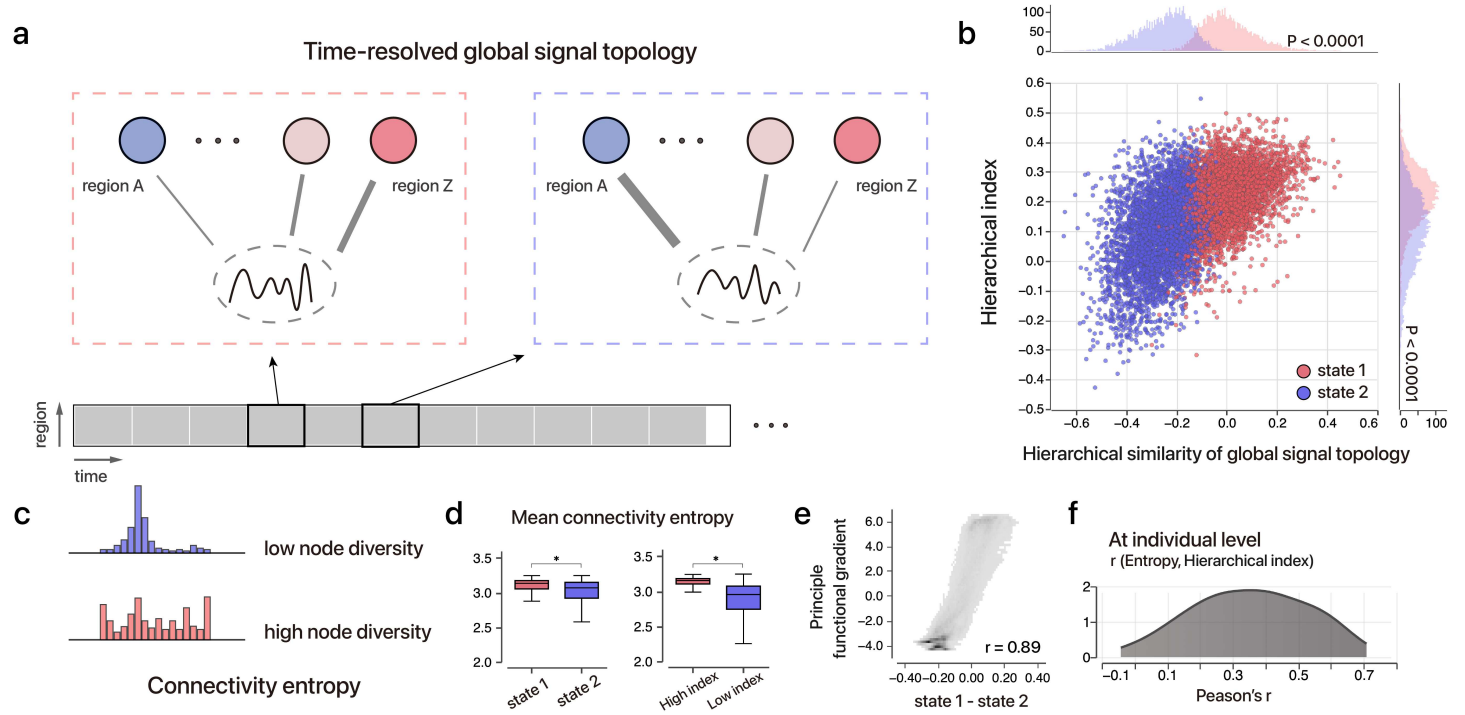
**a**, The hierarchical index distinguished the sedation state from wakefulness/recovery at the individual level (wakefulness versus sedation:  $t = 6.96, P < .01$ ; recovery versus sedation:  $t = 3.19, P < .01$ ; no significant difference was observed between wakefulness and recovery; paired sample  $t$ -test,  $n = 21$ ). **b**, top: Distribution of the tendency of the hierarchical index to drift during a ~15 min resting-state scanning in HCP data (982 individuals  $\times$  4 runs;  $* P < .05$ , unadjusted, Pearson trend test); a negative correlation indicates a decreasing trend during the scanning; bottom: partial correlation between the hierarchical index (averaged across four runs) and behavioural phenotypes. PC1 of reaction time and PSQI Component 3 were inverted for visualization (larger inter-individual hierarchical index corresponds to less reaction data and healthier sleep quality). **c**, The hierarchical index captures the temporal variation in sleep stages in each of six volunteers (grey line: scores by expert; blue line: hierarchical index; For subject 1:  $r = 0.78, P < .01$ ; For subject 2:  $r = 0.89, P < .01$ ; For subject 3:  $r = 0.78, P < .01$ ; For subject 4:  $r = 0.75, P < .01$ ; For subject 5:  $r = 0.79, P < .01$ ; For subject 6:  $r = 0.85, P < .01$ ; Pearson correlation). The vertical axis represents four sleep stages (wakefulness = 0, N1 = -1, N2 = -2, slow-wave sleep = -3) with time is shown on the horizontal axis (Subject 2 and Subject 4 were recorded for 6000 seconds; the others summed up to 6750 seconds); For the visualization, we normalized the hierarchical indexes across time and added the average value of the corresponding expert score. **d**, Distribution of the hierarchical index in the Myconnectome project. Sessions on Thursdays are shown in red colour (potentially high energetic states, unfasting / caffeinated) and sessions on Tuesdays in blue (fasting/uncaffeinated). Applying 0.2 as the threshold corresponding to a classification accuracy over 80% (20 of 22 Tuesday sessions surpassed 0.2; 20 in 22 Thursday sessions were of below 0.2) **e-f**, The hierarchical index can explain intra-individual variability in energy levels across different days (fatigue:  $r = -0.48, P < .01$ ; heightened attention:  $r = -0.49, P < .01$ ).

1 **Fig 3. Hierarchical index in psychedelic and psychotic brains.**



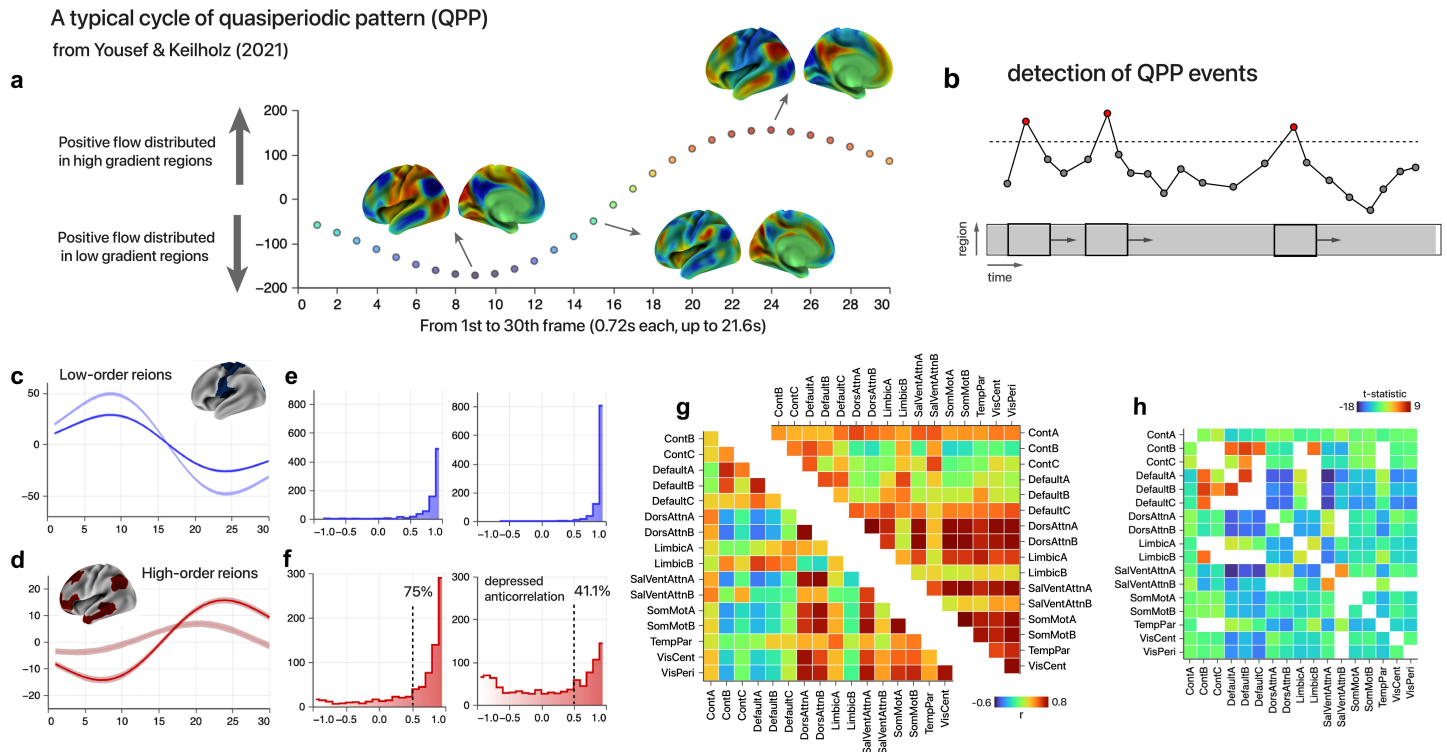
**a**, LSD effects on the hierarchical index across 15 healthy volunteers. fMRI images were scanned three times for each condition of LSD administration and a placebo. During the first and third scans, the subjects were in an eye-closed resting-state; during the second scan, the subjects were simultaneously exposed to music. \* (12 of 15 subjects) indicates that the hierarchical indexes were higher across three runs during the LSD administration than in the placebo condition. **b**, Left: Relationship between the hierarchical index and BPRS positive symptoms across 123 individuals with either ADHD, schizophrenia, or bipolar disorder ( $r = 0.25$ ,  $P = .0032$ ). Right: Correlation with each item in BPRS positive symptoms ( $*P < .05$ ). **c**, Left: the hierarchical index across different clinical groups from the UCLA dataset (SZ: schizophrenia, BP: bipolar disorder, HC: healthy control); Right: the hierarchical index across individuals with schizophrenia and healthy control from the PKU6 dataset.

**Fig 4. Complex and dynamic brain states unveiled by global signal topology and the hierarchical index during rest.**



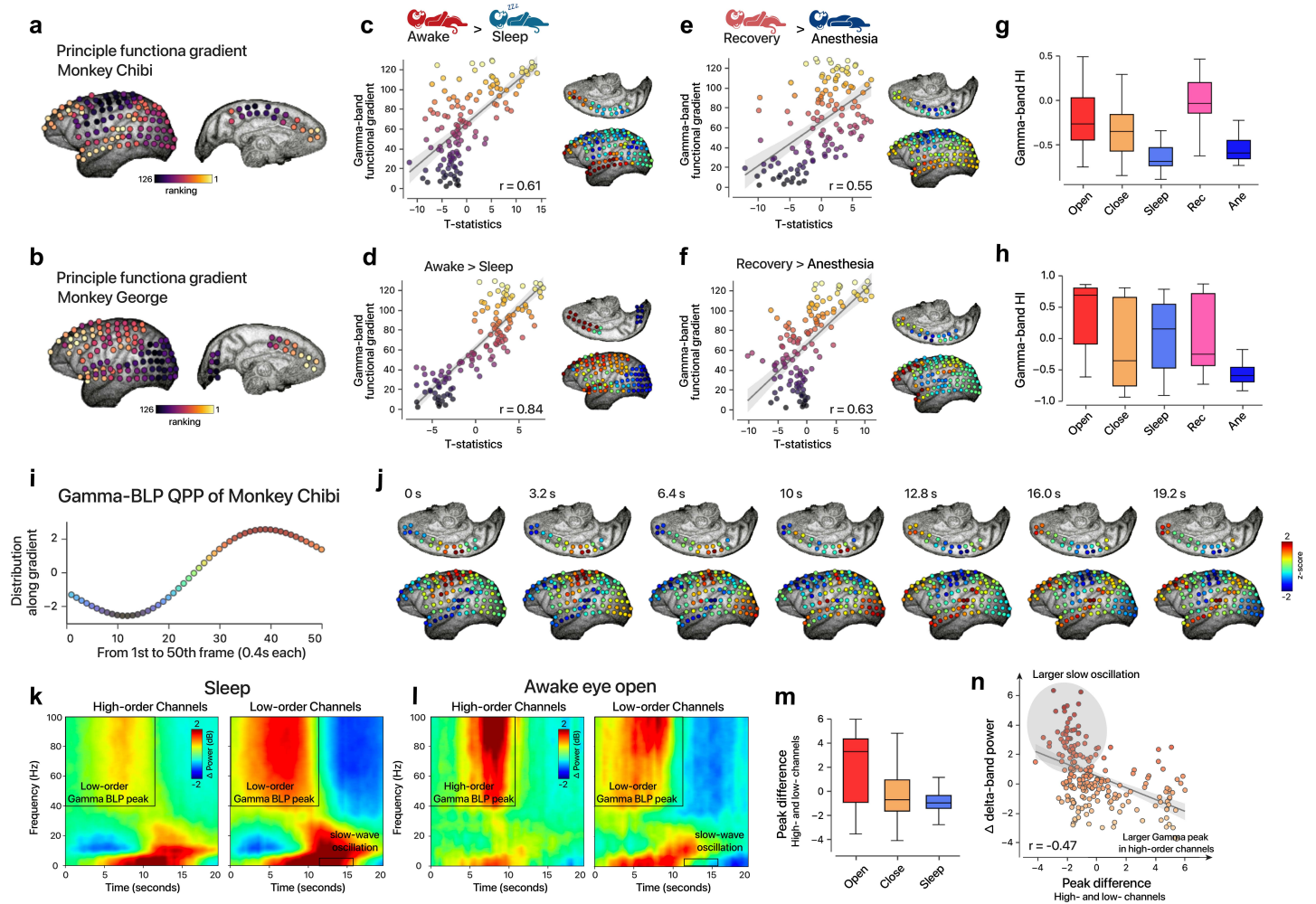
**a**, Simplified diagram for dynamic GS topology analysis. **b**, 2-cluster solution of the GS topology in 9,600 time windows from 100 unrelated HCP individuals. Scatter and distribution plots of the hierarchical index; the hierarchical similarity with the GS topology is shown. Each point represents a 35 s fragment. State 1 has significantly larger hierarchical index ( $P < .0001$ ) and hierarchical similarity with GS topology ( $P < .0001$ ) than State 2, indicating a higher level of vigilance and more association regions contributing to global fluctuations; meanwhile, the two variables are moderately correlated ( $r = 0.59$ ,  $P < .0001$ ). **c**, For a particular brain region, its connectivity entropy is characterized by the diversity in the connectivity pattern. **d**, Left: Higher overall connectivity entropy in State 1 than State 2 ( $P < .0001$ ). Right: Higher overall connectivity entropy in states with a higher hierarchical index (top 20% versus bottom 20%;  $P < .0001$ ). **e**, Difference in GS topology between State 1 and State 2 spatially recapitulates the principle functional gradient ( $r = 0.59$ ,  $P < .0001$ ), indicating that the data-driven GS transition moves along the cortical hierarchy. **f**, Distribution of Pearson's correlation between the hierarchical index and mean connectivity entropy across 96 overlapping windows (24 per run) across 100 individuals. In most individuals, the hierarchical index covaries with the diversity of the connectivity patterns (mean  $r = 0.386$ ).

**Fig 5. fMRI quasiperiodic pattern manifested in different vigilance states.**



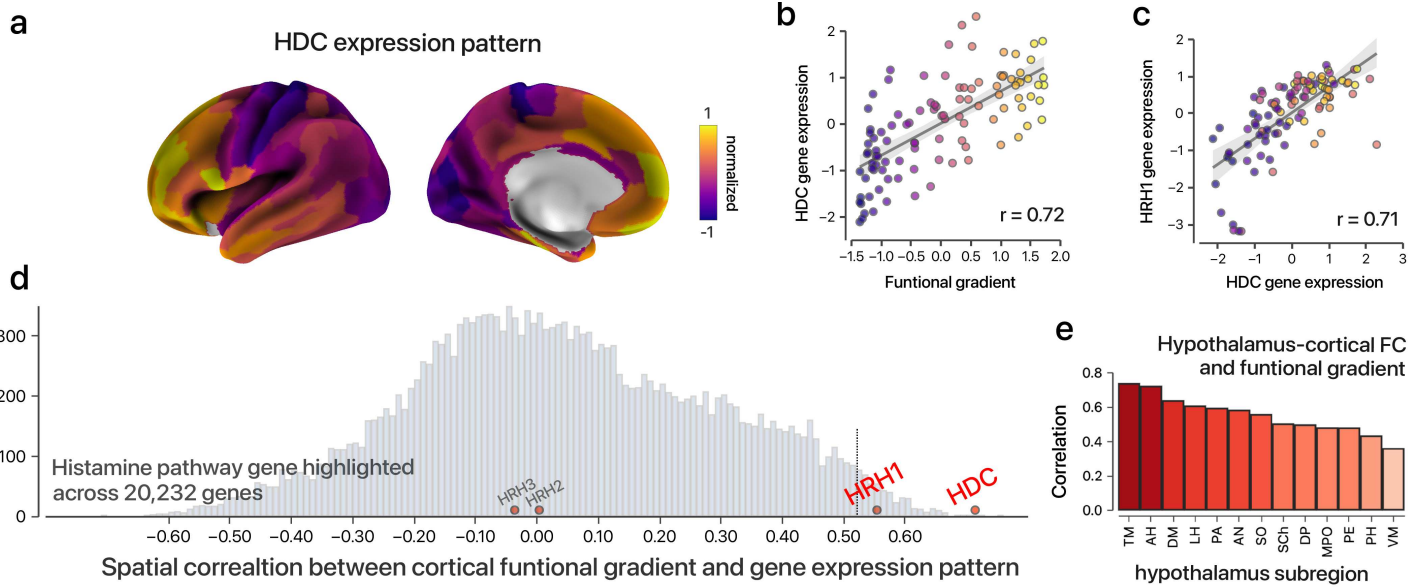
**a**, A cycle of spatiotemporal QPP reference from Yousef & Keilholz<sup>37</sup>; x-axis: HCP temporal frames (0.72 second each), y-axis: dot product of cortical BOLD values and principle functional gradient. Three representative frames were displayed: lower-order regions-dominated pattern (6.5 s), intermediate pattern (10.8 s) and associative regions-dominated pattern (17.3 s). **b**, A schematic diagram to detect QPP events in fMRI. The sliding window approach was applied to select spatiotemporal fragments, which highly resemble the QPP reference. **c-d**, Group-averaged QPP events detected in different vigilance states (initial and terminal 400 frames, respectively). For this visualization, the time series of the bottom 20% (c, blue) and top 20% (d, red) of the hierarchy regions were averaged across 30 frames. Greater saturability corresponds to the initial 400 frames with plausibly higher vigilance. **e-f**, Distribution of the temporal correlations between the averaged time series in the template and all the detected QPP events. Left: Higher vigilance; right: lower vigilance. For the top 20% multimodal areas, an  $r$  threshold of 0.5 was displayed to highlight the heterogeneity between the two states. **g**, Mean correlation map of Yeo 17 networks across QPP events in different vigilance states. Left: Higher vigilance; right: lower vigilance. **h**, Thresholded  $t$ -statistic map of Yeo 17 networks measuring the difference in Fig. 5g (edges with  $P < .05$  are shown).

**Fig 6. Hierarchical dynamics in macaque electrocortigraphy.**



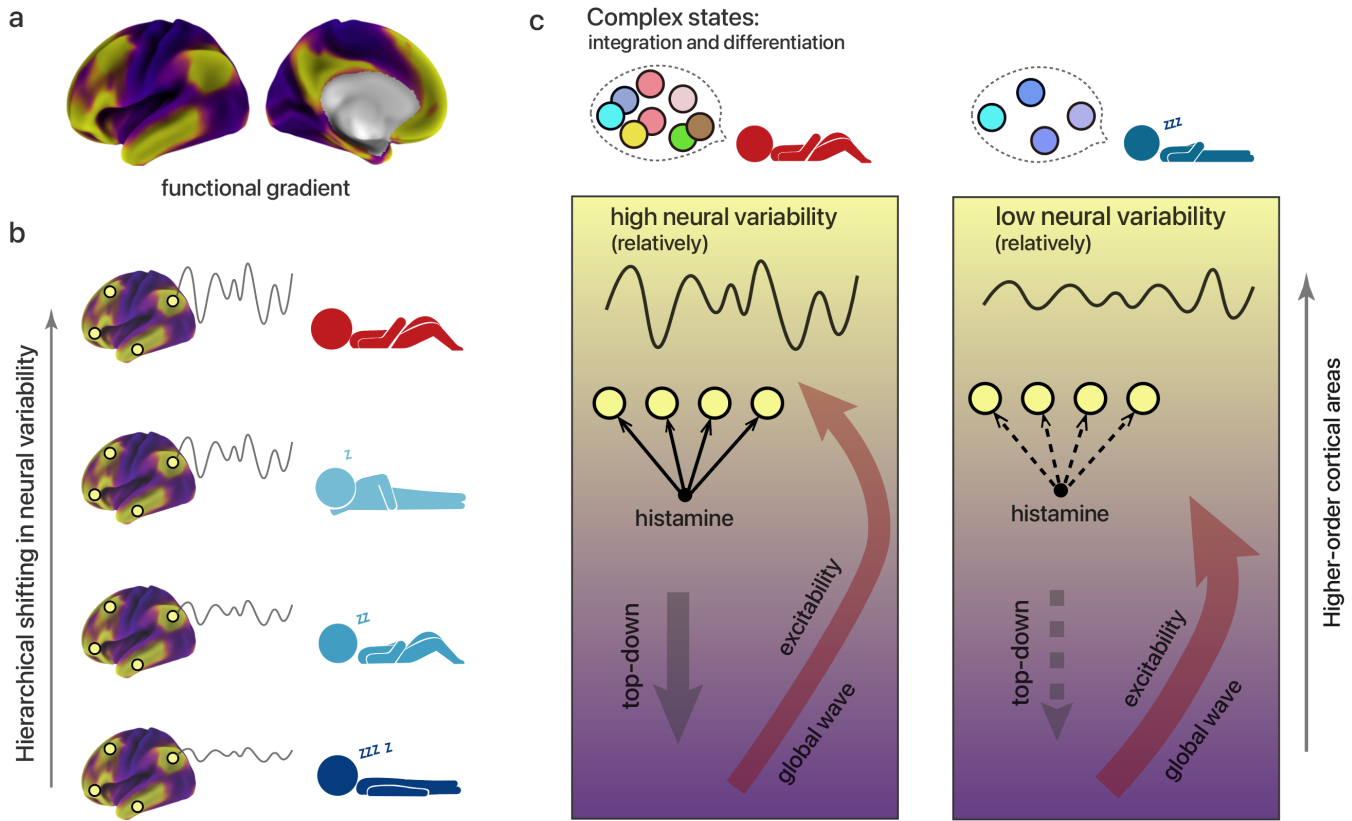
**a-b**, Principal embedding of gamma BLP connectome for Monkey *Chibi* and Monkey *George*. For this visualization, the original embedding value was transformed into a ranking index value for each macaque. **c-d**, Cortex-wide unthresholded *t*-statistical map of the sleep effect for Monkey C (**c**, left) and Monkey G (**d**, left). As in Fig. 1c,1f, and 1i, the principle functional gradient spatially associated with the sleep altered pattern (Monkey *Chibi*:  $r = 0.61$ ,  $P < .00001$ ; Monkey *George*:  $r = 0.84$ ,  $P < .00001$ ; Spearman rank correlation). **e-f**, Cortex-wide unthresholded *t*-statistical map of anesthesia effect for Monkey *Chibi* (**e**, left) and Monkey *George* (**f**, left). Principle functional gradient correlated with anesthesia-induced pattern (Monkey *Chibi*:  $r = 0.55$ ,  $P < .00001$ ; Monkey *George*:  $r = 0.63$ ,  $P < .00001$ ; Spearman rank correlation). **g-h**, Like Fig. 2, the hierarchical index was calculated for a fragment of the recording (here using 150 seconds) and could still differentiate distinct states of consciousness (From left to right: waking with eyes open, waking with eyes closed, sleeping, recovering from anesthesia, and anesthetized states). **i**, Like Fig. 5a, a typical cycle of gamma-BLP QPP in Monkey C; x-axis: HCP temporal frames (0.4 second each), y-axis: dot product of gamma-BLP values and principle functional gradient. **j**, Representative frames across 20 seconds. To better visualize the spatial topography, the mean value was subtracted in each frame across the typical gamma-BLP QPP template. **k-l**, Spectrogram averaged over high- and low-order electrodes (top 20%: left; bottom: right) in macaque C across several sleep recording (**k**) and awake eyes-open recording sessions. The results are highly analogous to the sequential spectral transition (SST) events. High gamma excitability is visually prominent in the preceding 12 s in the black block. **m**, Peak differences in gamma BLP between high- and low-order electrodes differentiate waking (eye-opened and eye-closed) and sleeping conditions (\* indicates  $P < .0001$ ; paired *T*-test). **n**, The peak difference in gamma BLP (in the initial 12 s) predicts the later 4 s nonoverlapping part of the change in average delta power across the cortex-wide electrodes ( $r = -0.47$ ,  $P < .0001$ , Monkey *Chibi*: awake eye-closed condition, Pearson correlation).

1 **Fig 7. Histaminergic system and hierarchical organization across the neocortex.**



3 **a**, Z-normalized map of the *HDC* transcriptional landscape based on the Allen Human Brain Atlas and the Human Brainnetome Atlas<sup>76</sup>.  
 4 **b-c**, Gene expression pattern of the *HDC* is highly correlated with functional hierarchy ( $r = 0.72$ ) and the expression of the *HRH1* gene  
 5 ( $r = 0.71$ ). **d**, Distribution of Spearman's Rho values across the gene expression of 20232 genes and the functional hierarchy. *HDC*  
 6 gene and histaminergic receptors genes are highlighted. **e**, Spatial association between hypothalamic subregions functional connection  
 7 to cortical area and functional gradient across 210 regions defined by Human Brainnetome Atlas. The tuberomammillary nucleus  
 8 showed one of the most outstanding correlations. From left to right: tuberomammillary nucleus (TM), anterior hypothalamic area (AH),  
 9 dorsomedial hypothalamic nucleus (DM), lateral hypothalamus (LH), paraventricular nucleus (PA), arcuate nucleus (AN),  
 10 suprachiasmatic nucleus (Sch), dorsal periventricular nucleus (DP), medial preoptic nucleus (MPO), periventricular nucleus (PE),  
 11 posterior hypothalamus (PH), ventromedial nucleus (VM).  
 12

1 **Fig 8. A Hypothetical Model for States of Consciousness.**



2  
3 **a**, Principal gradient of functional connectivity in the resting brain. Yellow versus violet represent high versus low loadings onto the low-  
4 dimensional gradient. **b**, A schematic diagram of our observations: Altered global state of consciousness associates with the  
5 hierarchical shift in cortical neural variability. **c**, Left: During vivid wakefulness, higher-order regions (yellow) exhibit disproportionately  
6 larger fluctuations, enabling complex global states in functional integration and differentiation. Such hierarchical heterogeneity is  
7 supported by spatiotemporal waves of excitability and by the histaminergic arousal system. Right: The breakdown of hierarchical  
8 heterogeneity facilitates the transition towards unconsciousness.

- 1 Northhoff, G., Wainio-Theberge, S. & Evers, K. Is temporo-spatial dynamics the “common currency” of brain and mind? In Quest of “Spatiotemporal Neuroscience”. *Physics of Life Reviews* vol. 33 (2020).
- 2 Northhoff, G. & Huang, Z. How do the brain’s time and space mediate consciousness and its different dimensions? Temporo-spatial theory of consciousness (TTC). *Neuroscience and Biobehavioral Reviews* vol. 80 (2017).
- 3 Fox, M. D. & Raichle, M. E. Spontaneous fluctuations in brain activity observed with functional magnetic resonance imaging. *Nature Reviews Neuroscience* vol. 8 (2007).
- 4 Berkes, P., Orbán, G., Lengyel, M. & Fiser, J. Spontaneous cortical activity reveals hallmarks of an optimal internal model of the environment. *Science (80-. )*. **331**, (2011).
- 5 Pezzulo, G., Zorzi, M. & Corbetta, M. The secret life of predictive brains: what’s spontaneous activity for? *Trends in Cognitive Sciences* vol. 25 (2021).
- 6 Maquet, P. *et al.* Default network connectivity reflects the level of consciousness in non-communicative brain-damaged patients. *Brain* **133**, 161–171 (2009).
- 7 Boveroux, P. *et al.* Breakdown of within- and between-network Resting State during Propofol-induced Loss of Consciousness. *Anesthesiology* (2010).
- 8 Tagliazucchi, E. *et al.* Breakdown of long-range temporal dependence in default mode and attention networks during deep sleep. *Proc. Natl. Acad. Sci. U. S. A.* **110**, 15419–15424 (2013).
- 9 Huang, Z., Zhang, J., Wu, J., Mashour, G. A. & Hudetz, A. G. Temporal circuit of macroscale dynamic brain activity supports human consciousness. *Sci. Adv.* (2020) doi:10.1126/sciadv.aaz0087.
- 10 Demertzi, A., Tagliazucchi, E., Dehaene, S., Deco, G. & Barttfeld, P. Human consciousness is supported by dynamic complex patterns of brain signal coordination. 1–12 (2019).
- 11 Luppi, A. I. *et al.* Consciousness-specific dynamic interactions of brain integration and functional diversity. *Nat. Commun.* (2019) doi:10.1038/s41467-019-12658-9.
- 12 Casali, A. G. *et al.* A theoretically based index of consciousness independent of sensory processing and behavior. *Science Translational Medicine* (2013) doi:10.1126/scitranslmed.3006294.
- 13 Barttfeld, P. *et al.* Signature of consciousness in the dynamics of resting-state brain activity. *Proc. Natl. Acad. Sci. U. S. A.* (2015) doi:10.1073/pnas.1418031112.
- 14 Waschke, L., Kloosterman, N. A., Obleser, J. & Garrett, D. D. Behavior needs neural variability. *Neuron* (2021) doi:10.1016/j.neuron.2021.01.023.
- 15 Uddin, L. Q. Bring the Noise: Reconceptualizing Spontaneous Neural Activity. *Trends Cogn. Sci.* **24**, 734–746 (2020).
- 16 Garrett, D. D. *et al.* Lost Dynamics and the Dynamics of Loss: Longitudinal Compression of Brain Signal Variability is Coupled with Declines in Functional Integration and Cognitive Performance. *Cereb. Cortex* **31**, (2021).
- 17 He, B. J. Scale-free properties of the functional magnetic resonance imaging signal during rest and task. *J. Neurosci.* **31**, (2011).
- 18 Tognoli, E. & Kelso, J. A. S. The Metastable Brain. *Neuron* **81**, 35–48 (2014).
- 19 Palva, S. & Palva, J. M. Roles of Brain Criticality and Multiscale Oscillations in Temporal Predictions for Sensorimotor Processing. *Trends in Neurosciences* vol. 41 (2018).
- 20 Ito, T. *et al.* Task-evoked activity quenches neural correlations and variability across cortical areas. *PLoS Comput. Biol.* (2020) doi:10.1371/JOURNAL.PCBI.1007983.
- 21 Churchland, M. M. *et al.* Stimulus onset quenches neural variability: A widespread cortical phenomenon. *Nat. Neurosci.* (2010) doi:10.1038/nn.2501.

- 1 22. Anderson, K. M. *et al.* Transcriptional and imaging-genetic association of cortical interneurons, brain function, and  
2 schizophrenia risk. *Nat. Commun.* **11**, (2020).
- 3 23. Wang, X. J. Macroscopic gradients of synaptic excitation and inhibition in the neocortex. *Nat. Rev. Neurosci.* (2020)  
4 doi:10.1038/s41583-020-0262-x.
- 5 24. Zou, Q. H. *et al.* An improved approach to detection of amplitude of low-frequency fluctuation (ALFF) for resting-state fMRI:  
6 fractional ALFF. *J Neurosci Methods* **172**, 137–141 (2008).
- 7 25. Thomas Yeo, B. T. *et al.* The organization of the human cerebral cortex estimated by intrinsic functional connectivity. *J.*  
8 *Neurophysiol.* **106**, (2011).
- 9 26. Poldrack, R. A. *et al.* Long-term neural and physiological phenotyping of a single human. *Nat. Commun.* **6**, (2015).
- 10 27. Sass, L. A. & Parnas, J. Schizophrenia, Consciousness and the Self. *Schizophrenia Bulletin* vol. 29 (2003).
- 11 28. Schartner, M. M., Carhart-Harris, R. L., Barrett, A. B., Seth, A. K. & Muthukumaraswamy, S. D. Increased spontaneous MEG  
12 signal diversity for psychoactive doses of ketamine, LSD and psilocybin. *Sci. Rep.* **7**, (2017).
- 13 29. Bayne, T. & Carter, O. Dimensions of consciousness and the psychedelic state. *Neurosci. Conscious.* **2018**, (2018).
- 14 30. Carhart-Harris, R. L. *et al.* Neural correlates of the LSD experience revealed by multimodal neuroimaging. *Proc. Natl. Acad.*  
15 *Sci. U. S. A.* **113**, 4853–4858 (2016).
- 16 31. Poldrack, R. A. *et al.* A phenome-wide examination of neural and cognitive function. *Sci Data* **3**, 160110 (2016).
- 17 32. Tononi, G., Boly, M., Massimini, M. & Koch, C. Integrated information theory: From consciousness to its physical substrate.  
18 *Nat. Rev. Neurosci.* **17**, 450–461 (2016).
- 19 33. Yang, G. J. *et al.* Altered Global Signal Topography in Schizophrenia. *Cereb. Cortex* (2017) doi:10.1093/cercor/bhw297.
- 20 34. Li, J. *et al.* Topography and behavioral relevance of the global signal in the human brain. *Sci. Rep.* **9**, (2019).
- 21 35. Tagliazucchi, E. & Laufs, H. Decoding Wakefulness Levels from Typical fMRI Resting-State Data Reveals Reliable Drifts  
22 between Wakefulness and Sleep. *Neuron* **82**, 695–708 (2014).
- 23 36. Raut, R. V. *et al.* Global waves synchronize the brain’s functional systems with fluctuating arousal. *Sci. Adv.* **7**, (2021).
- 24 37. Yousefi, B. & Keilholz, S. Propagating patterns of intrinsic activity along macroscale gradients coordinate functional  
25 connections across the whole brain. *Neuroimage* **231**, (2021).
- 26 38. Gu, Y. *et al.* Brain Activity Fluctuations Propagate as Waves Traversing the Cortical Hierarchy. *Cereb. Cortex* **31**, (2021).
- 27 39. Liu, X. *et al.* Arousal transitions in sleep, wakefulness, and anesthesia are characterized by an orderly sequence of cortical  
28 events. *Neuroimage* **116**, (2015).
- 29 40. Liu, X. *et al.* Subcortical evidence for a contribution of arousal to fMRI studies of brain activity. *Nat. Commun.* (2018)  
30 doi:10.1038/s41467-017-02815-3.
- 31 41. Di Perri, C. *et al.* Neural correlates of consciousness in patients who have emerged from a minimally conscious state: A cross-  
32 sectional multimodal imaging study. *Lancet Neurol.* **15**, (2016).
- 33 42. Mateo, C., Knutsen, P. M., Tsai, P. S., Shih, A. Y. & Kleinfeld, D. Entrainment of Arteriole Vasomotor Fluctuations by  
34 Neural Activity Is a Basis of Blood-Oxygenation-Level-Dependent “Resting-State” Connectivity. *Neuron* **96**, (2017).
- 35 43. Magri, C., Schridde, U., Murayama, Y., Panzeri, S. & Logothetis, N. K. The amplitude and timing of the BOLD signal reflects  
36 the relationship between local field potential power at different frequencies. *J. Neurosci.* **32**, (2012).
- 37 44. Nagasaka, Y., Shimoda, K. & Fujii, N. Multidimensional recording (MDR) and data sharing: An ecological open research and  
38 educational platform for neuroscience. *PLoS One* **6**, (2011).
- 39 45. Yanagawa, T., Chao, Z. C., Hasegawa, N. & Fujii, N. Large-scale information flow in conscious and unconscious states: An  
40 ECoG study in monkeys. *PLoS One* **8**, (2013).
- 41 46. Neudorfer, C. *et al.* A high-resolution in vivo magnetic resonance imaging atlas of the human hypothalamic region. *Sci. Data*

7, (2020).

47. González-García, C. & He, B. J. A gradient of sharpening effects by perceptual prior across the human cortical hierarchy. *J. Neurosci.* **41**, (2021).
48. Boly, M. *et al.* Preserved feedforward but impaired top-down processes in the vegetative state. *Science (80-. )*. **332**, (2011).
49. Horga, G. & Abi-Dargham, A. An integrative framework for perceptual disturbances in psychosis. *Nature Reviews Neuroscience* vol. 20 (2019).
50. Tononi, G., Boly, M., Massimini, M. & Koch, C. Integrated information theory: From consciousness to its physical substrate. *Nature Reviews Neuroscience* (2016) doi:10.1038/nrn.2016.44.
51. Mashour, G. A., Roelfsema, P., Changeux, J. P. & Dehaene, S. Conscious Processing and the Global Neuronal Workspace Hypothesis. *Neuron* **105**, 776–798 (2020).
52. He, J. H. *et al.* Hyperactive external awareness against hypoactive internal awareness in disorders of consciousness using resting-state functional MRI: Highlighting the involvement of visuo-motor modulation. *NMR Biomed.* **27**, (2014).
53. Orban, C., Kong, R., Li, J., Chee, M. W. L. & Yeo, B. T. T. Time of day is associated with paradoxical reductions in global signal fluctuation and functional connectivity. *PLoS Biol.* **18**, (2020).
54. Liu, T. T., Nalci, A. & Falahpour, M. The global signal in fMRI: Nuisance or Information? *Neuroimage* **150**, (2017).
55. Fukunaga, M. *et al.* Large-amplitude, spatially correlated fluctuations in BOLD fMRI signals during extended rest and early sleep stages. *Magn. Reson. Imaging* (2006) doi:10.1016/j.mri.2006.04.018.
56. Yellin, D., Berkovich-Ohana, A. & Malach, R. Coupling between pupil fluctuations and resting-state fMRI uncovers a slow build-up of antagonistic responses in the human cortex. *Neuroimage* **106**, (2015).
57. Liu, X., Leopold, D. A. & Yang, Y. Single-neuron firing cascades underlie global spontaneous brain events. *Proc. Natl. Acad. Sci. U. S. A.* **118**, (2021).
58. Yoshikawa, T., Nakamura, T. & Yanai, K. Histaminergic neurons in the tuberomammillary nucleus as a control centre for wakefulness. *British Journal of Pharmacology* vol. 178 (2021).
59. Yu, X. *et al.* Wakefulness Is Governed by GABA and Histamine Cotransmission. *Neuron* **87**, (2015).
60. Turchi, J. *et al.* The Basal Forebrain Regulates Global Resting-State fMRI Fluctuations. *Neuron* **97**, (2018).
61. Burt, J. B. *et al.* Hierarchy of transcriptomic specialization across human cortex captured by structural neuroimaging topography. *Nat. Neurosci.* (2018) doi:10.1038/s41593-018-0195-0.
62. Deco, G., Vidaurre, D. & Kringelbach, M. L. Revisiting the global workspace orchestrating the hierarchical organization of the human brain. *Nat. Hum. Behav.* (2021) doi:10.1038/s41562-020-01003-6.
63. Signorelli, C. M., Uhrig, L., Kringelbach, M., Jarraya, B. & Deco, G. Hierarchical disruption in the cortex of anesthetized monkeys as a new signature of consciousness loss. *Neuroimage* **227**, (2021).
64. Yeshurun, Y., Nguyen, M. & Hasson, U. The default mode network: where the idiosyncratic self meets the shared social world. *Nat. Rev. Neurosci.* **22**, (2021).
65. Levinson, M., Podvalny, E., Baete, S. H. & He, B. J. Cortical and subcortical signatures of conscious object recognition. *Nat. Commun.* **12**, (2021).
66. González-García, C., Flounders, M. W., Chang, R., Baria, A. T. & He, B. J. Content-specific activity in frontoparietal and default-mode networks during prior-guided visual perception. *Elife* **7**, (2018).
67. Raut, R. V., Snyder, A. Z. & Raichle, M. E. Hierarchical dynamics as a macroscopic organizing principle of the human brain. *Proc. Natl. Acad. Sci. U. S. A.* (2020) doi:10.1073/pnas.2003383117.
68. Wagner, U., Gais, S., Haider, H., Verleger, R. & Born, J. Sleep inspires insight. *Nature* (2004) doi:10.1038/nature02223.
69. Prince, L. Y. & Richards, B. A. The overfitted brain hypothesis. *Patterns* **2**, (2021).

- 1 70. Zhang, J. *et al.* Altered global signal topography and its different regional localization in motor cortex and hippocampus in  
2 mania and depression. *Schizophr. Bull.* **45**, (2019).
- 3 71. Li, R. *et al.* Shared and distinct global signal topography disturbances in subcortical and cortical networks in human epilepsy.  
4 *Hum. Brain Mapp.* **42**, (2021).
- 5 72. Zhang, J., Huang, Z., Tumati, S. & Northoff, G. Rest-task Modulation of fMRI-derived Global Signal Topography is Mediated  
6 by Transient Co-activation Patterns. *bioRxiv* 798819 (2020) doi:10.1101/798819.
- 7 73. Preller, K. H. *et al.* Changes in global and thalamic brain connectivity in LSD-induced altered states of consciousness are  
8 attributable to the 5-HT<sub>2A</sub> receptor. *Elife* **7**, 1–31 (2018).
- 9 74. Li, J. *et al.* Global Signal Regression Strengthens Association between Resting-State Functional Connectivity and Behavior.  
10 (2019).
- 11 75. Bayne, T., Hohwy, J. & Owen, A. M. Are There Levels of Consciousness? *Trends Cogn. Sci.* **20**, 405–413 (2016).
- 12 76. Fan, L. *et al.* The Human Brainnetome Atlas: A New Brain Atlas Based on Connectional Architecture. *Cereb Cortex* **26**,  
13 3508–3526 (2016).
- 14  
15  
16  
17  
18  
19  
20  
21  
22  
23  
24  
25  
26  
27  
28  
29  
30  
31  
32  
33  
34  
35  
36  
37  
38  
39  
40  
41  
42  
43  
44  
45  
46  
47  
48

# Methods

## Data and Preprocessing

### *Dataset 1: Dexmedetomidine-induced Sedation*

21 healthy male volunteers (age:  $26.4 \pm 2.1$  years; right-handed; body mass index:  $21.7 \pm 1.9$ ) were recruited from Capital Medical University, Beijing, China. To ensure the safety of the experiment, all included volunteers were at an American Society of Anesthesiologists (ASA) physical status I or II. The exclusion criteria included: (1) the presence of metal implants in the body, (2) the presence of intracranial lesions or systemic comorbidities, (3) a history of general anesthesia, (4) a history of drug abuse or alcohol abuse, (5) an allergy to dexmedetomidine, (6) claustrophobia, and/or (7) left-handedness. The experiment protocol was approved by the Institutional Review Board of Beijing Tiantan Hospital, Capital Medical University, China. After being informed of the relevant details of the study, all subjects signed written informed consent to their participation. More details can be found in our registered clinical trial at [clinicaltrials.gov](https://clinicaltrials.gov) (registration number: *NCT03343873*).

All volunteers were instructed to fast before the experiment (at least 6 hours from solids and 2 hours from liquids). Due to its minor effect on respiratory inhibition, dexmedetomidine was used as the anesthetic drug to induce the sedation states. Specifically, dexmedetomidine was administered through an intravenous catheter inserted into a vein in the right hand, initially with a bolus at  $1 \mu\text{g}/\text{kg}/\text{h}$  over 15 min and subsequently by a  $0.6 \mu\text{g}/\text{kg}/\text{h}$  continuous intravenous infusion to maintain sedation. Simultaneous, continuous monitoring, including heart rate, arterial pressure, pulse oxygen saturation, respiratory rate, and electrocardiography, was applied throughout all the experiments (Supplementary Table 6). The Observer's Assessment of Alertness/Sedation (OAA/S) scale and Ramsay sedation scale (RSS) were used to evaluate the sedation level. The subjects were judged to be awake or to be fully recovered if they responded readily to verbal commands or to their name being spoken in a normal tone (RSS score of 2; OAA/S scale score of 5). Subjects were judged to be under moderate sedation if they had lethargic responses to verbal commands and to their name being spoken in a normal tone or if they responded only after their name was called loudly (RSS score of 3–4; OAA/S scale score of 3–4). RSS and OAA/S scale verbal commands were repeated twice during each assessment. All the subjects wore headphones throughout the experiment and were thus spoken to through an MRI speaker. All communications occurred between MRI acquisitions, and the subjects were instructed to respond verbally. These operations were conducted by two certified anesthesiologists with complete resuscitation equipment available.

Resting-state fMRI data were recorded using an echo-planar imaging (EPI) sequence in a Siemens Medical Systems Prisma 3.0 T MRI system at Beijing Neurosurgical Institute. The scanning parameters were as follows:  $\text{TR} = 2000$  ms;  $\text{TE} = 30$  ms; field-of-view =  $192 \times 192 \text{ mm}^2$ ; acquisition matrix =  $64 \times 64$ ; flip angle =  $75^\circ$ ; slice thickness = 4 mm; voxel size =  $3 \times 3 \times 4.4 \text{ mm}^3$ . The subjects were scanned for 6 minutes 40 s across each of the three conscious states: normal wakefulness (RSS score, 2; OAA/S Scale score, 5), moderate sedation (RSS score, 3–4; OAA/S Scale score, 3–4), and recovery of consciousness (RSS score, 2; OAA/S Scale score, 5).

1 The fMRI data were preprocessed using an open-access MATLAB toolbox BRANT v3.35<sup>1</sup> (<https://github.com/kbxu/brant>).  
2 The standardized pipeline included: i) slice timing correction, fixing the temporal shifts of different slices; ii) within-subject  
3 EPI image realignment, estimating and spatially correcting for head motions; iii) spatial normalization to the Montreal  
4 Neurological Institute (MNI) standard space and resampling to a  $3 \times 3 \times 3 \text{ mm}^3$  resolution; iv) nuisance regression,  
5 regressors included linear trends, averaged signals, and their first-order temporal derivatives within the white matter and  
6 cerebrospinal fluid regions, as well as Friston's 24 head motion parameters<sup>2</sup> (3 rotation and 3 translation parameters, 6  
7 parameters one time point before, and the 12 corresponding squared items); v) bandpass filtering, the residuals of the  
8 regression models were bandpass-filtered (0.01–0.08 Hz) to further suppress low-frequency drifts and physiological noises  
9 such as breathing and heartbeat.

### 11 ***Dataset 2: 3T Resting-state fMRI***

12 The resting-state fMRI data was acquired as part of the HCP S1200 release<sup>3</sup>. We analysed functional imaging data acquired  
13 from a 3T Siemens Skyra scanner using multiband EPI. Participants with 4 runs of resting-state data were included: 4 runs  
14 in REST1 and REST2 session with right-to-left (run 1 and run 3) and left-to-right (run 2 and run 4) phase encoding. Each  
15 run lasted 14 min and 33 s (TR = 720 ms; TE = 33.1 ms; field-of-view =  $208 \times 180 \text{ mm}^2$ ; acquisition matrix =  $104 \times 90$ ;  
16 flip angle =  $52^\circ$ ; slice thickness = 2 mm; voxel size =  $2 \times 2 \times 2 \text{ mm}^3$ ). Within-scanner sleep during resting-state scanning is  
17 commonly reported. Based on a previous study that used combined EEG-fMRI trained classifiers during sleep stages, nearly  
18 one third of subjects were determined to have not maintained their wakefulness for over 3 minutes<sup>4</sup>. Thus, we speculate that  
19 subjects were predisposed to decreased alertness when close to the end of scanning. Although such speculation cannot be  
20 generalized to all individuals, such an effect could be overwhelming at the population level.

22 Resting-state fMRI data was processed based on the HCP-pipeline using the CIFTI grayordinate-based framework, and  
23 spatially structured physiological noise was corrected using the ICA+FIX method, which can be assessed in the HCP  
24 repository. Such an ICA-based approach<sup>5</sup> is effective for cleaning structured noise and provided a different denoising  
25 strategy beyond nuisance regression in this research. The signal was further cleaned with a Butterworth filter within 0.01-  
26 0.08 Hz. Finally, 982 individuals with complete four resting state runs without large motion (mean framewise distance <  
27 0.3 mm) were included in our study. The description of the behavioural phenotypes in HCP was detailed elsewhere<sup>6</sup>. Items  
28 belonging to alertness (Pittsburgh Sleep Questionnaire), in-scanner task performance, and cognition were selected for  
29 further analyses. To summarize the overall reaction time of the in-scanner tasks, the principal component analysis was  
30 conducted to items that tapped to reaction times (such as median reaction time during tasks; with more than 950 individuals  
31 available). Only the first PC was used because it explained 30.8% of the variance and positively correlated with all the items  
32 included, whereas the second PC only explained 17% of the variance.

### 34 ***Dataset 3: Simultaneous EEG-fMRI during sleeping***

36 Young healthy volunteers (18 - 25 years) were enrolled via online advertisement. To ensure their safety, participants with a  
37 history of any psychiatric or neurological illness were excluded from the experiment; and participants with normal sleep

1 quality were considered according to the Pittsburgh Sleep Quality Index (PSQI). Each subject provided written informed  
2 consent after a detailed explanation of the study protocol. No intake of alcohol or caffeine was allowed on the scanning day.  
3 The sleeping experiment started at approximately 01: 00 local time. Each participant was asked to lie down and fall asleep  
4 on the scanner bed. The experimenter checked the participant's sleeping condition through a microphone every eight  
5 minutes. The response of the participant was recorded through an MRI-compatible multiple button-press box. Participants  
6 who failed to sleep did not continue with the experiment. The 2 hours of sleeping scanning (nine 12.5 min runs) did not start  
7 until the participants were nonresponsive. All experiments were in accordance with the Declaration of Helsinki. The study  
8 protocol was approved by the Ethics Committee of Southwest University, China.

9  
10 Sleep fMRI data were acquired using a 3T Siemens Trio scanner at the Sleep and Neuroimaging Center at Southwest  
11 University, Chongqing, Beijing. Head movements were minimized by using a cushioned head fixation device. A T2-  
12 weighted gradient echo-planar imaging (EPI) sequence was applied, with the scanning parameters as follows: TR = 1500  
13 ms; TE = 29 ms; field-of-view =  $192 \times 192 \text{ mm}^2$ ; acquisition matrix =  $64 \times 64$ ; flip angle =  $90^\circ$ ; slice thickness = 5 mm;  
14 voxel size =  $3 \times 3 \times 5.5 \text{ mm}^3$ . To access sleep stages during fMRI scanning, simultaneous EEG-fMRI recordings were  
15 conducted by a 32-channel MRI-compatible Brain Products system (BrainAmp MR plus, Brain products, Munich,  
16 Germany). The channel position was in accordance with the international 10/20 system, and all impedances were below 10  
17 k $\Omega$ . The FCz point was used as the reference for online signal collection, and the sampling rate was 5 kHz. To ensure the  
18 temporal stability of the EEG acquisition in relation to the switching of the gradients during the MR acquisition, we used a  
19 SyncBox (SyncBox MainUnit, Brain Products GmbH, Gilching, Germany) to synchronize the amplifier system with the  
20 MRI scanner's system. The EEG amplifier was a non-magnetic MRI-compatible EEG system and was charged by a  
21 rechargeable power pack placed outside the scanner bore. The amplified and digitized EEG signal was transmitted to the  
22 recording computer with fiber optic cables. The computer was placed outside the scanner room, and the adapter (BrainAmp  
23 USB-Adapter, Brain products, Gilching, Germany) converted the optical signal into an electric signal.

24  
25 Sleeping fMRI data was preprocessed based on the BRANT standardized pipeline. The original EEG recording was  
26 processed using the Vision-Analyzer software (Version 2.0, Brain Products, Inc., Munich, Germany). Applying the average  
27 template subtraction procedure, we first removed the fMRI gradient and ballistocardiographic artifacts from the original  
28 EEG signal. Then the EEG data were down-sampled to 250 Hz and digitally filtered within the 0.1-45 Hz band using a  
29 Chebyshev II-type filter. Furthermore, the residual fMRI gradient and ballistocardiographic artifacts, ocular artifacts, and  
30 the muscle activity artifact from the EEG data were eliminated through temporal independent component analysis (ICA).  
31 After removing severe artifacts, six EEG channels (O1, O2, F3, F4, C3, C4) were selected for manual sleep staging by two  
32 experts, with a time window of 30 seconds. Each segmented epoch was classified into awake, N1, N2, or slow-wave sleep  
33 condition according to the 2017 AASM manual<sup>7</sup>. Then, the 6 (out of 22) volunteers with the most consistent sleeping  
34 trajectories, as labelled by two experts, were included in the further analyses.

#### 35 36 ***Dataset 4: the MyConnectome Project***

1 We downloaded the raw resting-state fMRI and behavioural data of the MyConnectome Project<sup>8</sup> from a public database  
2 OpenNeuro (<https://openneuro.org/datasets/ds000031/versions/00001>), comprising a deeply sampled phenotyping of a  
3 single individual (a Caucasian male; 45 years old at study; right-handed) over a period of 18 months. Scan sessions 14–104  
4 were included in the analysis (84 sessions according to a previous work<sup>8</sup>), which were from the original acquisition period  
5 of the study using a Siemens Skyra 3T scanner at the University of Texas. In each session, 10 minutes of resting-state data  
6 were acquired using a multiband EPI sequence, with the following parameters: TR = 1160 ms; TE = 30 ms; field-of-view  
7 = 240 × 240 mm<sup>2</sup>; acquisition matrix = 96 × 96; flip angle = 63°; voxel size = 2.4 × 2.4 × 2 mm<sup>3</sup>, 68 slices (64 slices after  
8 session 27). The fMRI data was pre-processed using the BRANT standardized pipeline but without the option of slice timing  
9 correction.

10  
11 The Myconnectome Project provides a unique opportunity to study the longitudinal, intra-individual effects of physical and  
12 psychological factors on brain function. Scans were mostly performed on either Tuesdays or Thursdays at 0730 hours.  
13 Before each Tuesday scan, the subject fasted and had no caffeine intake; on Thursdays, the subject was always fed and  
14 caffeinated. Thus, we inferred that the subject was in a relatively low state of energy both physically and psychologically  
15 during the Tuesday scans. To quantify the brain state linking to a neuroimaging session, we also assessed the self-reported  
16 Positive and Negative Affect Schedule (PANAS-X) questionnaires, which was administered after each scan. Referenced  
17 from a previous work<sup>9</sup>, the arousal factors were categories associated with fatigue (average scores: “drowsy”: Q28; “sleepy”:  
18 Q57; “sluggish”: Q58; and “tired”: Q62) or heightened attention (average scores: “attentive”: Q11; “concentrating”: Q18;  
19 and “lively”: Q43) and were further compared across the different days.

### 21 ***Dataset 5: Psychedelic State***

22 The functional imaging data for the psychedelic state was collected and analysed in a previous study<sup>10</sup> and was recently  
23 made available on the OpenNeuro platform (<https://openneuro.org/datasets/ds003059>). This resource included 15 healthy  
24 volunteers who were all examined under conditions of both placebo and LSD administration. In these two conditions, each  
25 individual was scanned three times: the first and third runs were a common eyes-closed resting-state paradigm, and the  
26 second scan was accompanied by listening to music. More information about data acquisition and preprocessing can be  
27 found elsewhere<sup>10</sup>. Briefly, a gradient echo planer imaging sequence was used to acquire BOLD-weighted fMRI data (TR  
28 = 2000 ms, TE = 35 ms, field-of-view = 220 mm, acquisition matrix = 64 × 64, parallel acceleration factor = 2, flip angle =  
29 90°). 35 oblique axial slices were acquired in an interleaved fashion, each 3.4 mm thick with zero slice gap (3.4 mm isotropic  
30 voxels). Each BOLD scan lasted seven minutes. Because the released data did not include raw functional MRI images, we  
31 used the preprocessed data directly. Notably, this preprocessed pipeline rigidly controlled head motion using de-spiking,  
32 motion-related nuisance regression, and band-pass filtering (0.01-0.08 Hz) and has been demonstrated to have minimal  
33 motion effect on functional connectivity<sup>10</sup>.

### 34 35 ***Dataset 6: Neuropsychiatric Disorders***

36 We assessed data from the UCLA Consortium for Neuropsychiatric Phenomics<sup>11</sup> from the OpenNeuro platform (<https://openneuro.org/datasets/ds000030/>). Specifically, 117 healthy subjects, 47 individuals with schizophrenia, 45 individuals

1 with bipolar disorder, and 41 individuals with ADHD were included in our study. All participants were asked to give written  
2 informed consent for their inclusion, following procedures approved by the Institutional Review Boards at UCLA and the  
3 Los Angeles County Department of Mental Health. All patients were conducted with behavioural and symptom assessments,  
4 including the Brief Psychiatric Rating Scale (BPRS). Resting-state data was scanned using an echo planar imaging (EPI)  
5 sequence from a 3T Siemens Syngo scanner at UCLA (TR = 2000 ms, TE = 30 ms, field-of-view = 192 mm, acquisition  
6 matrix =  $64 \times 64$ , flip angle =  $90^\circ$ , voxel size =  $3 \times 3 \times 4 \text{ mm}^3$ , 34 slices), lasting for 304 seconds. In addition, 92 individuals  
7 diagnosed with schizophrenia and 98 matched healthy controls, whose data were collected from Peking University Sixth  
8 Hospital, China, were further analysed for an independent validation. A consensus diagnosis of schizophrenia was made by  
9 two experienced senior psychiatrists according to the Diagnosis and Statistic Manual of Mental Disorders, fourth edition  
10 (DSM-IV) criteria for schizophrenia or schizophreniform disorder and finally diagnosed with schizophrenia after being  
11 followed up for at least six months. All patients had significant positive symptoms: more than four on at least three of seven  
12 positive items based on the Positive and Negative Syndrome Scale. The study protocol was approved by the Medical  
13 Research Ethics Committees of the local hospitals and written informed consent was obtained from all participants and/or  
14 their legal guardians. Detailed clinical information was provided in our previous work<sup>12</sup>. 8 minutes of resting-state fMRI  
15 data were acquired using an EPI sequence with the following parameters: TR = 2000 ms; TE = 30 ms; acquisition matrix  
16 =  $64 \times 64$ ; flip angle =  $90^\circ$ ; slice thickness = 4 mm; voxel size =  $3.4375 \times 3.4375 \times 4.6 \text{ mm}^3$ ). The fMRI preprocessing  
17 (UCLA and PKU6) is based on the BRANT platform and can be found elsewhere<sup>12</sup>. Subjects with high motion during the  
18 scanning were excluded (translation  $>3 \text{ mm}$  or rotation  $>3^\circ$ ).

### 19 20 ***Dataset 7: Macaque ECoG Data***

21 We downloaded the macaque electrophysiological recordings from a publicly available database (<http://neurotycho.org>).  
22 The acquisition details and experimental procedures can be found in previous publications<sup>13,14</sup>. Briefly, a chronically  
23 implanted customized 128-channel ECoG electrode array was employed to record neural activity in the left hemisphere.  
24 The sampling rate was 1 kHz using the Cerebus data acquisition system (Blackrock, UT, USA). We analysed the ECoG  
25 data from two adult macaque monkeys (*Chibi: Macaca fuscata*; *George: Macaca mulatta*) acquired under different  
26 conditions: the awake, eyes-closed resting-state (*Chibi*: in 12 sessions, lasting 150 minutes; *George*: in 13 sessions, lasting  
27 153 minutes), the awake, eyes-opened resting-state (*Chibi*: in 12 sessions, lasting 164 minutes; *George*: in 12 sessions,  
28 lasting 148 minutes), the sleeping state (*Chibi*: in 7 sessions, lasting 326 minutes; *George*: in 6 sessions, lasting 233 minutes),  
29 the anesthetized state (*Chibi*: in 8 sessions, lasting 132 minutes; *George*: in 9 sessions, lasting 117 minutes), as well as the  
30 eyes-opened, recovered state (*Chibi*: in 7 sessions, lasting 96 minutes; *George*: in 9 sessions, lasting 109 minutes). Some  
31 sessions were labelled with more than one condition, and each condition lasted more than 5 minutes. Under the sleep state,  
32 the experimental room was kept quiet and dark for up to 1.5 hours, and the monkeys were conducted to sit calmly with an  
33 eye mask. Slow wave oscillation appeared intermittently during natural sleep. Immediately following the sleep condition,  
34 the eyes-closed condition was collected with the light turned on. For the eyes-open waking state, there was no eye mask. In  
35 the anesthesia experiment, several agents (ketamine, medetomidine, or propofol) were applied to induce loss of  
36 consciousness; and the anesthetized state was collected after a monkey no longer responded to manipulation of the monkey's  
37 hand or to touching the nostril or philtrum with a cotton swab.

1  
2 The line noise was removed at 50 Hz and its harmonics using notch filtering. According to the previous work, two channels  
3 from monkey *Chibi* were excluded due to stubborn artifacts. The multitaper spectral estimation was applied to generate  
4 spectrograms for 1-100 Hz power in 1 Hz frequency bins. The window size was 1 s (0.2 s step size), and the number of  
5 tapers was set to 5. Next, we transformed the power spectrogram into decibels using a logarithmic function and normalized  
6 each frequency bin by removing the temporal mean of the power. Band-limited power (BLP) was calculated by averaging  
7 the normalized spectrogram within defined frequency ranges: delta 1–4 Hz; alpha-beta 5–30 Hz and gamma 40–100 Hz.  
8 BLP signals were further bandpass-filtered (0.01–0.08 Hz) using the Butterworth approach, and a forward-backward digital  
9 filter was implemented to eliminate any phase delay.

### 11 ***Dataset 8: High-resolution 7T Resting-state fMRI Data***

12 To finely characterize the functional connectivity of the hypothalamic system, we applied resting-state fMRI data, which  
13 were acquired from a 7T Siemens Magnetom scanner using a multiband sequence in HCP. 176 participants with 4 full  
14 resting-state runs were included: 4 runs in REST1 and REST2 session with posterior-to-anterior (run 1 and run 3) and  
15 anterior-to-posterior (run 2 and run 4) phase encoding. Each run lasted 16 minutes (TR = 1000 ms; TE = 22.2 ms; field-of-  
16 view =  $208 \times 208 \text{ mm}^2$ ; acquisition matrix =  $130 \times 130$ ; flip angle =  $45^\circ$ ; slice thickness = 1.6 mm; voxel size =  $1.6 \times 1.6 \times$   
17  $1.6 \text{ mm}^3$ ). We started our analyses used on 7T preprocessed fMRI data after ICA FIX-cleaned in the HCP repository, and  
18 volume-based images were used to cover the full hypothalamus. The preprocessed fMRI data retained a spatial resolution  
19 of  $1.6 \times 1.6 \times 1.6 \text{ mm}^3$  and was a part of HCP new release in 2018, which had been fixed from the incorrect unwrapped  
20 direction in the fMRIVolume pipeline.

21  
22 A recently developed hypothalamic atlas<sup>15</sup> was applied to delineate the segmentation of the hypothalamus, including 13  
23 hypothalamic structures: anterior hypothalamic area, arcuate nucleus, dorsal periventricular nucleus, dorsomedial  
24 hypothalamic nucleus, lateral hypothalamus, medial preoptic nucleus, paraventricular nucleus, periventricular nucleus,  
25 posterior hypothalamus, suprachiasmatic nucleus, supraoptic nucleus, tuberomammillary nucleus, and ventromedial nucleus.  
26 Considering the potential spatial mismatch of small hypothalamic divisions, we performed a binary dilation for each  
27 subregion with a cube connectivity of 1 to moderately expand the shape, resulting in 75 voxels (from 18 voxels,  
28 tuberomammillary nucleus) with a spatial resolution of  $1.6 \times 1.6 \times 1.6 \text{ mm}^3$ . The time series within the dilated hypothalamic  
29 mask were averaged. For the cortical regions, we derived voxel-wise time series based on fMRI data smoothed with a 6  
30  $\text{mm}^3$  FWHM kernel. All signals were temporally cleaned by a Butterworth filter within 0.01-0.08 Hz. Subsequently, the  
31 voxel-wise FC between the hypothalamic divisions and the cerebral cortex was calculated by Pearson's correlation for each  
32 run and averaged across all 176 individuals.

### 34 **BOLD variability**

35  
36 It has recently been proposed that moment-to-moment brain signal variability is more informative than static metrics such  
37 as mean signal values<sup>16</sup>. We calculated BOLD variability (also termed low-frequency BOLD amplitude) as the standard

1 deviation of temporally filtered time series (0.01-0.08 Hz), at the voxel-/vertex-wise level. The frequency band is a default  
 2 parameter in the standardized BRANT pipeline. Based on Parseval's theorem, such a temporal metric is mathematically  
 3 analogous to the amplitude of low-frequency fluctuations (ALFF) calculated in the frequency domain<sup>17</sup>:

$$\begin{aligned}
 X(t) &= \sum_{k=1}^N [a_k \cos(2\pi f_k t) + b_k \sin(2\pi f_k t)] \\
 ALFF &= \sum_{k: f_k \in [0.01, 0.08]} \sqrt{\frac{a_k^2(f) + b_k^2(f)}{N}}
 \end{aligned}$$

### 7 **Three Consciousness-related Maps**

8 We tested whether the consciousness-related pattern of the BOLD signal amplitude was consistent across different  
 9 paradigms. Importantly, to characterize the spatial heterogeneity, rather than using an overall absolute value, the amplitude  
 10 map was normalised into a z-score at the voxel/vertex level. Specifically, the HCP resting-state fMRI data was analysed  
 11 across all the cortical surface vertices in the CIFTI format, and the anesthesia and sleep fMRI data were analysed across the  
 12 cortical voxels in MNI space. In this way, three cortex-wide maps were generated and spatially compared using fMRI data  
 13 collected under anesthesia, during sleep, and in the resting state:

14  
 15 *Dexmedetomidine-induced sedation.* The map in Figure 1b was formed using the *t*-statistic values between the z-score  
 16 BOLD amplitudes in sedation and wakefulness using a paired sample *t* test ( $n = 21$ , FWHM = 6 mm<sup>3</sup>). The pattern is highly  
 17 consistent with that obtained using the contrast between states in sedation and recovery (Supplementary Fig. 2).

18  
 19 *Vigilance decrease.* The map in Figure 1e was formed using the Spearman's rank *r* between the z-score BOLD amplitude  
 20 and the time interval. Practically, each HCP run was divided into 24 non-overlapping time windows of 50 frames each, and  
 21 then the pairwise difference in amplitude was calculated. This approach resulted in up to 1,225 differed maps for each run,  
 22 with the time interval ranging from 1 to 23 intervals. The larger interval was inferred to have a higher possibility of a  
 23 decrease in vigilance. Collectively, for each cortical grayordinate, the Spearman's rank *r* was calculated using 4,914,700  
 24 ( $1,225 \times 4$  runs  $\times$  982 individuals) points.

25  
 26 *Sleep.* The map in Figure 1h was formed using the Spearman's rank correlation between the z-score BOLD amplitude and  
 27 the sleep stages manually labelled by an expert (15 s interval; Wakefulness: 0 > N1 stage: -1 > N2 stage: -2 > Slow-wave  
 28 sleep stage: -3). Data from six volunteers was concatenated in the temporal resolution of 50 frames (75 s, FWHM = 6 mm<sup>3</sup>),  
 29 and the sleep score was calculated by simply averaging across the five labelled sleep stages (from 0, -1, -2, or -3).

### 31 **Hierarchy Analysis**

#### 32 *Definition of Cortical Hierarchy / Gradient*

1 Cortex-wide maps of the principal FC diffusion values and T1w/T2w ratios were used to characterize the macroscale  
2 hierarchical organization of the human brain. The principal FC diffusion, also called principle functional gradient, represents  
3 the main area of variance in functional connectivity and is spatially locating along the sensorimotor-to-transmodal axis. The  
4 functional gradient was calculated via diffusion map embedding, a non-linear manifold learning approach, on the group-  
5 level dense functional connectome matrix. The embedded space was constructed by an appropriately random walk process  
6 on a pairwise cosine similarity graph of dense coordinate's FC pattern. The algorithm is controlled by the parameter  $\alpha = 0.5$ ,  
7 which can balance the global and local relationship between nodes constructed in the embedded space. The eigenvectors of  
8 the transition matrix on this graph were defined as diffusion coordinates. The detailed procedures were described in  
9 Margulies *et al*<sup>18</sup>. The first eigenvector can explain the greatest variance (more than 25%) in HCP resting-state fMRI data  
10 and was assessed from publicly available results from Margulies *et al*. T1w/T2w ratio mapping was downloaded from the  
11 HCP S1200 Group Average Data Release ([https://www.humanconnectome.org/study/hcp-young-adult/article/s1200-](https://www.humanconnectome.org/study/hcp-young-adult/article/s1200-group-average-data-release)  
12 [group-average-data-release](https://www.humanconnectome.org/study/hcp-young-adult/article/s1200-group-average-data-release)). The T1w/T2w map was proposed as an in vivo measure to index the grey-matter myelin  
13 content and anatomical hierarchy.

### 14 ***Diffusion Map for Macaque***

15 To achieve an individual-level principal gradient for the gamma-band connectome, we used the BrainSpace toolbox<sup>19</sup> (<https://github.com/MICA-MNI/BrainSpace>)  
16 implemented in Python. Consistent with previous work<sup>20</sup>, we analysed fMRI data  
17 obtained during the awake, eye-closed resting state. First, a functional connectivity matrix was established via computing  
18 the pairwise Pearson's correlation between the time series of the gamma-band power across channels. A cosine kernel was  
19 then used to construct an affinity matrix for the averaged FC map across sessions for each macaque. The diffusion map was  
20 conducted using the pipeline described above based on BrainSpace (diffusion embedding,  $\alpha = 0.5$ , sparsity = 0.9). The  
21 generated diffusion maps of the two macaques were visually analogous to those found in a previous work<sup>20</sup>.

### 22 ***Hierarchical index***

23 The hierarchical index was defined as the Spearman's Rho between the principle functional gradient and the normalized  
24 low-frequency BOLD amplitude across the entire cortex. This simple indicator describes how spontaneous fluctuations shift  
25 along the macroscale functional hierarchy across time. For the volume-based fMRI data (Dataset 1 and Datasets 3-6), the  
26 surface-based gradient in HCP fsLR32k was transformed into MNI volumetric space using the '-metric-to-volume-mapping'  
27 command in Connectome Workbench, using the ribbon constrained mapping algorithm option. The ribbon gradient map in  
28 MNI space was spatially equivalent to the image released in NeuroVault from Margulies *et al*<sup>18</sup>. ( $r > 0.99$ , <https://neurovault.org/images/24346/>).

### 29 **Complex Brain State Analysis**

30 We hypothesized that the low-dimension flow of the hierarchical index is associated with distinct brain states during rest.  
31 To test this hypothesis, we divided the 1200 frames of each HCP run into 24 non-overlapped 35 s windows across 100  
32 unrelated individuals (up to 9,600 fragments) to explore the tempo-spatial heterogeneity of global signal topology as well  
33 as brain complexity. The same procedure was performed using only fragments that had a lower head motion (mean

1 framewise distance < 0.1 mm) and another 100 unrelated individuals, and the findings were highly robust (Supplementary  
2 Figure 4).

### 3 4 ***Unsupervised Learning of GS topology***

5 Here, we calculated the time-resolved GS topology in each non-overlapped window. The global signal was defined as the  
6 average BOLD signal across all the cortical vertexes. A GS topography map was calculated using the Pearson correlation  
7 between the global signal and the time series for each grayordinate of the cortex. Subsequently, the spatial correlation of  
8 the GS topology between each fragment was calculated as a  $9,600 \times 9,600$  similarity matrix, and a data-driven K-means  
9 algorithm with Euclidean distance was applied. A two-cluster solution was applied, given its larger silhouette coefficient  
10 metric (from 2 to 10 clusters). Notably, the intention of the unsupervised learning was not to demonstrate that brain states  
11 are perfectly natural clusters but to decompose spatially heterogeneous patterns of GS topologies across time and individuals.  
12

### 13 ***Connectivity and Temporal Entropy***

14 To assess the cortical functional connectome, we applied the 200 parcellation Schaefer atlas<sup>22</sup> to downsample the dimension  
15 of the time series. For each non-overlapping window of an individual, we acquired a  $200 \times 200$  similarity matrix defined  
16 by the Pearson's correlation between each pair of Schaefer ROIs. Connectivity entropy was then used to describe the  
17 distribution diversity of the functional connectivity. To quantify the amount of uncertainty in each brain state, we adopted  
18 Saenger et al.'s method<sup>23</sup> to transform the functional connectivity values for each node into discrete bins ( $n = 10$ ) and  
19 calculated the normalized the Shannon entropy for each ROI's probability distribution. The connectivity entropy was  
20 calculated according to the following equation:  
21

$$22 \quad H = - \sum_{i=1}^n \frac{p_i \log(p_i)}{\log(n)}$$

23 In addition, we used sample entropy to measure the regularity and complexity of the temporal fluctuation. Specifically, the  
24 timeseries was divided into chunks of  $m$  or  $m + 1$  timepoints each. The chunks were then compared to find the Chebyshev  
25 distance between them. The parameter  $r$  was set as the threshold to determine whether two chunks were similar. The sample  
26 entropy was defined as:

$$27 \quad H = - \log \frac{A}{B}$$

28 in which  $A$  is the number of chunks of length  $m + 1$  having a Chebyshev distance less than  $r$  ( $B$  refers to the number of  
29 similar chunks of length  $m$ ). We used  $m = 2$  considering the length of time ( $N$  less than  $10^m$ ), and  $r = 0.5$  multiplied by the  
30 standard deviation of time series accounting for the amplitude variations of signals. Such parameters were previously used  
31 in resting-state fMRI studies<sup>24,25</sup>.  
32

### 33 **Recurring Spatiotemporal Pattern Analysis**

34

1 Spontaneous BOLD fluctuations manifest as one of a few recurring spatiotemporal patterns. Of these, one of the most  
2 investigated is a quasiperiodic pattern (QPP) described by Majeed et al<sup>26</sup>. This QPP was identified by recursively matching  
3 and averaging similar segments of resting-state fMRI time series. The primary QPP involves a dynamic cycle of activation  
4 and deactivation that spatially follows the macroscale gradient (from the task positive network to the default mode network)  
5 and lasts approximately 20 seconds. For the human fMRI data, we directly applied a representative spatiotemporal template  
6 to match all possible QPP events. This template is publicly available (<https://github.com/GT-EmoryMINDlab>) from a recent  
7 study<sup>27</sup> that conducted an optimized, computationally expensive algorithm to detect QPP events based on HCP S900 subjects.  
8 Only cortical regions were included when generating this group template. Consistent with this previous work<sup>27</sup>, we applied  
9 a sliding window approach to iteratively compare the correlation between the template (30 volumes, ~21.6 seconds) and  
10 each flattened ‘segment’ with a temporal step of 1 TR. To reduce computational complexity, we analysed the ROI-based  
11 average time series to identify QPP events using the Schaefer 200 parcellation map. Spatiotemporal segments were  
12 identified as QPP events whose local maxima exceeded the threshold ( $r = 0.4$ ). In this analysis, our purpose was not to  
13 demonstrate the cortex-wide propagation pattern or its role in arousal modulation, which have been revealed previously, but  
14 to study whether the previously reported QPP exhibits significant heterogeneous modes in different vigilance states. To  
15 achieve this, 100 HCP individuals with the most protruding drifts in hierarchical scores during 4 resting-state scans were  
16 included. For each of 400 scans (100 individuals  $\times$  4 runs), the first third and the last third of the time were categorized into  
17 two different vigilance states. In this way, we were able to perform the QPP analysis on 400 high-quality fMRI scans in two  
18 different global states while avoiding introducing individual difference.

19  
20 We next conducted an exploratory QPP analysis for the filtered gamma-band (40-100 Hz) power from the macaque ECoG  
21 recordings. For each macaque, we established a representative spatiotemporal template during the awake, eyes-closed  
22 resting state, considering: i) previous studies that suggested arousal shifts were linked to global fMRI signals in the eyes-  
23 closed condition, and ii) that the template could be independently used to detect QPP events in other states (such as during  
24 sleeping and eyes-opened condition) for comparing QPP heterogeneity. We downsampled the temporal resolution into 0.4  
25 s, and 50 timepoints (20 s) were then set as the segment duration. Based on the C-PAC package, a standard QPP algorithm  
26 was applied to reveal the recurrent spatiotemporal patterns ([https://github.com/FCP-INDI/C-  
27 PAC/blob/main/CPAC/qpp/qpp.py](https://github.com/FCP-INDI/C-PAC/blob/main/CPAC/qpp/qpp.py)). A threshold  $r$  of 0.4 was used when building the template. Practically, the results were  
28 not sensitive to thresholds of  $r$  from 0.2–0.5. We found that the QPP templates could be reliably derived and were visually  
29 similar in the two monkeys. To match the QPP templates from the two monkeys, we applied a phase-adjusting procedure  
30 by shifting a few timepoints forward and backward. As shown in Fig 6j and Supplementary Fig 6, the QPP template resulted  
31 in the propagation of activity along the macroscale functional gradient. Across the 50 timepoints, the weighted signals along  
32 the principle functional embedding achieved a high temporal correlation ( $r = 0.99$ ) between the two monkeys. The QPP  
33 template for each macaque was subsequently used to detect QPP events in other states. In each QPP event, we calculated  
34 the gamma BLP peak difference between the top and bottom 20 channels based on the cortical gradient to quantify the  
35 relative excitability of the high-order cortex. The peak difference was calculated within the initial 12 s when the gamma  
36 BLP was most evident, and the delta signals in the subsequent 4 s were averaged across all channels.

## Imaging Transcriptomic Analysis

To examine which transcriptomic expression recapitulates the cortex-wide map of the functional hierarchy, we assessed the Allen Human Brain Atlas (AHBA)<sup>28</sup>, a spatially comprehensive dataset of human transcriptional profiles. The gene expression data were acquired from post-mortem tissues in six donors without a history of psychiatric or neuropathological disorders. The donors were a 24-year-old African American male (H0351.2001), a 39-year-old African American male (H0351.2002), a 57-year-old European-ancestry male (H0351.1009), a 31-year-old European-ancestry male (H0351.1012), a 49-year-old Hispanic female (H0351.1015), and a 55-year-old European-ancestry male (H0351.1016). Further details are provided at <http://www.brain-map.org>.

Instead of the Schaefer atlas, the Human Brainnetome Atlas<sup>29</sup> was applied here to spatially define the samples because it was developed in volumetric space and reveals anatomical connectivity patterns. We then aligned the gene expression data from the AHBA dataset into the 105 left cortical regions defined in the Human Brainnetome Atlas, using the standard workflow embedded in the abagen toolbox<sup>30</sup>. Specifically, the probe that exhibited the most consistent pattern of regional variation across donors was selected to index the gene expression. Using a scaled robust sigmoid normalization approach, expression values within each brain sample were normalized across genes and then normalized for each gene across samples for each donor. The anatomical information for the left cortex was used to match the hemisphere and tissue class designation provided by AHBA. Finally, the average normalized values of all samples encompassed within each parcel was defined in the left hemisphere Human Brainnetome Atlas, resulting in 105 expression values for each of 20,232 genes across the left cortex. The spatial association between the gene expression and the functional gradient across 105 brain regions was calculated by Spearman's rank correlation.

1. Xu, K., Liu, Y., Zhan, Y., Ren, J. & Jiang, T. BRANT: A Versatile and Extendable Resting-State fMRI Toolkit. *Front Neuroinform* **12**, 52 (2018).
2. Friston, K. J., Williams, S., Howard, R., Frackowiak, R. S. & Turner, R. Movement-related effects in fMRI time-series. *Magn Reson Med* **35**, 346–355 (1996).
3. Smith, S. M. *et al.* Resting-state fMRI in the Human Connectome Project. *Neuroimage* (2013) doi:10.1016/j.neuroimage.2013.05.039.
4. Tagliazucchi, E. & Laufs, H. Decoding Wakefulness Levels from Typical fMRI Resting-State Data Reveals Reliable Drifts between Wakefulness and Sleep. *Neuron* **82**, 695–708 (2014).
5. Salimi-Khorshidi, G., Douaud, G., Beckmann, C. F., Glasser, M. F., Griffanti, L. & Smith, S. M. Automatic denoising of functional MRI data: Combining independent component analysis and hierarchical fusion of classifiers. *Neuroimage* **90**, (2014).
6. Van Essen, D. C. *et al.* The Human Connectome Project: A data acquisition perspective. *NeuroImage* vol. 62 (2012).
7. Berry, R. B., Brooks, R., Gamaldo, C., Harding, S. M., Lloyd, R. M., Quan, S. F., Troester, M. T. & Vaughn, B. V. AASM scoring manual updates for 2017 (version 2.4). *Journal of Clinical Sleep Medicine* vol. 13 (2017).
8. Poldrack, R. A. *et al.* Long-term neural and physiological phenotyping of a single human. *Nat. Commun.* **6**, (2015).
9. Shine, J. M., Koyejo, O. & Poldrack, R. A. Temporal metastates are associated with differential patterns of time-resolved connectivity, network topology, and attention. *Proc. Natl. Acad. Sci. U. S. A.* **113**, (2016).
10. Carhart-Harris, R. L. *et al.* Neural correlates of the LSD experience revealed by multimodal neuroimaging. *Proc. Natl. Acad. Sci. U. S. A.*

1 **113**, 4853–4858 (2016).

- 2 11. Poldrack, R. A., Congdon, E., Triplett, W., Gorgolewski, K. J., Karlsgodt, K. H., Mumford, J. A., Sabb, F. W., Freimer, N. B., London, E.  
3 D., Cannon, T. D. & Bilder, R. M. A phenome-wide examination of neural and cognitive function. *Sci Data* **3**, 160110 (2016).
- 4 12. Li, A. *et al.* A neuroimaging biomarker for striatal dysfunction in schizophrenia. *Nat. Med.* (2020) doi:10.1038/s41591-020-0793-8.
- 5 13. Yanagawa, T., Chao, Z. C., Hasegawa, N. & Fujii, N. Large-scale information flow in conscious and unconscious states: An ECoG study in  
6 monkeys. *PLoS One* **8**, (2013).
- 7 14. Nagasaka, Y., Shimoda, K. & Fujii, N. Multidimensional recording (MDR) and data sharing: An ecological open research and educational  
8 platform for neuroscience. *PLoS One* **6**, (2011).
- 9 15. Neudorfer, C., Germann, J., Elias, G. J. B., Gramer, R., Boutet, A. & Lozano, A. M. A high-resolution in vivo magnetic resonance imaging  
10 atlas of the human hypothalamic region. *Sci. Data* **7**, (2020).
- 11 16. Waschke, L., Kloosterman, N. A., Obleser, J. & Garrett, D. D. Behavior needs neural variability. *Neuron* (2021)  
12 doi:10.1016/j.neuron.2021.01.023.
- 13 17. Zuo, X. N., Di Martino, A., Kelly, C., Shehzad, Z. E., Gee, D. G., Klein, D. F., Castellanos, F. X., Biswal, B. B. & Milham, M. P. The  
14 oscillating brain: Complex and reliable. *Neuroimage* **49**, (2010).
- 15 18. Petrides, M., Huntenburg, J. M., Smallwood, J., Ghosh, S. S., Falkiewicz, M., Goulas, A., Jefferies, E., Eickhoff, S. B., Langs, G.,  
16 Castellanos, F. X., Margulies, D. S. & Bezgin, G. Situating the default-mode network along a principal gradient of macroscale cortical  
17 organization. *Proc. Natl. Acad. Sci.* **113**, 12574–12579 (2016).
- 18 19. Vos de Wael, R., Benkarim, O., Paquola, C., Lariviere, S., Royer, J., Tavakol, S., Xu, T., Hong, S. J., Langs, G., Valk, S., Mistic, B.,  
19 Milham, M., Margulies, D., Smallwood, J. & Bernhardt, B. C. BrainSpace: a toolbox for the analysis of macroscale gradients in  
20 neuroimaging and connectomics datasets. *Commun. Biol.* **3**, (2020).
- 21 20. Raut, R. V., Snyder, A. Z., Mitra, A., Yellin, D., Fujii, N., Malach, R. & Raichle, M. E. Global waves synchronize the brain's functional  
22 systems with fluctuating arousal. *Sci. Adv.* **7**, (2021).
- 23 21. Margulies, D. S., Ghosh, S. S., Goulas, A., Falkiewicz, M., Huntenburg, J. M., Langs, G., Bezgin, G., Eickhoff, S. B., Castellanos, F. X.,  
24 Petrides, M., Jefferies, E. & Smallwood, J. Situating the default-mode network along a principal gradient of macroscale cortical  
25 organization. *Proc. Natl. Acad. Sci. U. S. A.* (2016) doi:10.1073/pnas.1608282113.
- 26 22. Schaefer, A., Kong, R., Gordon, E. M., Laumann, T. O., Zuo, X.-N., Holmes, A. J., Eickhoff, S. B. & Yeo, B. T. T. Local-Global  
27 Parcellation of the Human Cerebral Cortex from Intrinsic Functional Connectivity MRI. *Cereb. Cortex* **28**, (2018).
- 28 23. Saenger, V. M., Ponce-Alvarez, A., Adhikari, M., Hagmann, P., Deco, G. & Corbetta, M. Linking entropy at rest with the underlying  
29 structural connectivity in the healthy and lesioned brain. *Cereb. Cortex* **28**, (2018).
- 30 24. Omidvarnia, A., Zalesky, A., Mansour L, S., Van De Ville, D., Jackson, G. D. & Pedersen, M. Temporal complexity of fMRI is  
31 reproducible and correlates with higher order cognition. *Neuroimage* **230**, (2021).
- 32 25. McDonough, I. M. & Nashiro, K. Network complexity as a measure of information processing across resting-state networks: Evidence from  
33 the Human Connectome Project. *Front. Hum. Neurosci.* **8**, (2014).
- 34 26. Majeed, W., Magnuson, M., Hasenkamp, W., Schwarb, H., Schumacher, E. H., Barsalou, L. & Keilholz, S. D. Spatiotemporal dynamics of  
35 low frequency BOLD fluctuations in rats and humans. *Neuroimage* **54**, (2011).
- 36 27. Yousefi, B. & Keilholz, S. Propagating patterns of intrinsic activity along macroscale gradients coordinate functional connections across the  
37 whole brain. *Neuroimage* **231**, (2021).
- 38 28. Hawrylycz, M. J. *et al.* An anatomically comprehensive atlas of the adult human brain transcriptome. *Nature* **489**, 391–399 (2012).
- 39 29. Fan, L., Li, H., Zhuo, J., Zhang, Y., Wang, J., Chen, L., Yang, Z., Chu, C., Xie, S., Laird, A. R., Fox, P. T., Eickhoff, S. B., Yu, C. & Jiang,  
40 T. The Human Brainnetome Atlas: A New Brain Atlas Based on Connectional Architecture. *Cereb Cortex* **26**, 3508–3526 (2016).
- 41 30. Markello, R. D., Arnatkevičiūtė, A., Poline, J. B., Fulcher, B. D., Fornito, A. & Mistic, B. Standardizing workflows in imaging  
42 transcriptomics with the Abagen toolbox. *Elife* **10**, (2021).
- 43  
44  
45  
46  
47

1  
2  
3  
4  
5  
6  
7  
8  
9  
10  
11  
12  
13  
14  
15  
16  
17

**Acknowledgements**

This work was supported by the Natural Science Foundation of China (Grant number 82171543), the Strategic Priority Research Program of the Chinese Academy of Sciences (XDB32020200), and the Start-up Funding of Beijing Normal University. We thank Rhoda E. and Edmund F. Perozzi, PhDs for English, and content editing assistance.

**Author contributions**

B.L., and X.W., led the project. R.H., H.L., X.L., C.Z., and H.Y. contributed to the data collection. A.L., B.L. and X.W. designed the study and wrote the manuscript. A.L. analyzed the data. R.H., H.L., X.L., Y.H., Q. Wu, Y.Y., X.Z., X.T., P.Y., and Q. Wang interpreted the data. S.H., Y.H. and Q. Wu provided critical comments. All authors edited and proofread the manuscript.

**Competing interests**

The authors declare no competing interests.

## Supplementary Files

This is a list of supplementary files associated with this preprint. Click to download.

- [SupplementaryFinal.pdf](#)